POLITECNICO DI TORINO
Repository ISTITUZIONALE

Managing transport properties in composite electrodes/electrolytes for all-solid-state lithium-based batteries

(Article begins on next page)

20 April 2024

Journal Name

ARTICLE

Managing transport properties in composite electrodes/electrolytes for all-solid-state lithium-based batteries

Marisa Falco[a], Stefania Ferrari[b], Giovanni Battista Appetecchi[c], and Claudio Gerbaldi[a,*]

In the global competition for ultimate electrochemical energy storage systems, the international tendency of Original Equipment Manufacturers (OEM) is to consider more and more the solid state technology as a solution that could replace the current Li-ion battery operating with liquid electrolytes. The reason is the need of enhanced energy density batteries, which are also durable and inherently safe. The proper understanding of the interfacial properties within and with the electrode materials is of paramount importance for the purpose. Indeed, all-solid-state lithium-based secondary batteries require efficient ion conductive pathways through the whole electrode thickness, to properly access all the active material particles, thus providing full electrode capacity. In this respect, here we propose an overview on the strategies adopted to achieve this goal, covering polymeric and inorganic ion conductors and composites thereof, their preparation procedures and characterisation techniques, which nowadays represent utmost important topics in the academic/industrial community to provide solutions for the shortcomings of safety, low ion mobility and cycle life.

Introduction

The pressing demand for long lasting, high power portable electronics, and the emerging large-scale diffusion of electric vehicles (EVs) and energy storage from renewables, require lower cost and improved energy density batteries, with enhanced cycle life and safety.[1] Lithium ion batteries (LIBs) currently on the market contain liquid electrolytes (LEs), that are cheap, easy to prepare and ensure optimum wetting of the electrodes, thus enabling ionic pathways throughout the whole thickness of the cell and minimising the internal resistance.[2] Anyway, in a bid to achieve higher energy density, using high potential cathode materials (> 4.5 V vs Li$^+$/Li) in cells with LEs may result in unwanted reactions despite the use of additives, thus compromising the stability and operational life.[3] Moreover, the attempt to reduce the thickness of the separator below 10 μm can result in safety issues, as in the case of recent problems with Samsung Note 7.[1,4] Additional limitations of LEs include difficulties to achieve flexible cell designs, risk of leakage and flammability, restricted thermal stability and low Li$^+$ transference

number (t_{Li+}, viz. the fraction of Li$^+$ ion conductivity with respect to the overall ionic conductivity σ_i), leading to cell polarisation.[1]

Within this context, a variety of solid-state electrolytes have been investigated so far being the development of ion-conducting materials for application in batteries one of the most active research areas in solid-state electrochemistry. Solid electrolytes (SEs) offer an alternative to avoid battery failures due to the use of organic electrolytes in LEs, thus favouring the transition from conventional LIBs to all-solid-state batteries (ASBs) (see *Figure 1*). In principle SEs make possible to extend the operating temperature range of a device, assuring higher safety even in the case of fire, together with high energy and power density.

At present, the large-scale ASBs available on the market contain only solid polymer electrolytes (SPEs), as in the case of the poly(ethylene oxide) (PEO)-based electrolyte in lithium metal polymer batteries (LMPB) powering Bolloré Blue car.[5] In SPEs, the ionic conduction occurs through polymer movements; the Li$^+$ ions hop from one void to another that are formed during local rearrangements of polymer chain segments. Polymers can combine amorphous and crystalline domains, and the prevailing conduction mechanism is usually ascribed to the segmental motion in the amorphous regions, although there are some reports about LiXF$_6$-PEO systems (X = Sb, As, P) where the conductivity of the crystalline phase has been found to be relatively high.[6,7]

[a] *Group for Applied Materials and Electrochemistry (GAME Lab), Department of Applied Science and Technology (DISAT), Politecnico di Torino, Corso Duca degli Abruzzi 24, 10129 Torino, Italy*

[b] *Department of Pharmacy, University of Chieti–Pescara "G. d'Annunzio", Via dei Vestini 31, 66100 Chieti, Italy*

[c] *ENEA, Agency for New Technologies, Energy and Sustainable Economic Development, SSPT-PROMAS-MATPRO, Via Anguillarese 301, Rome, 00123, Italy*

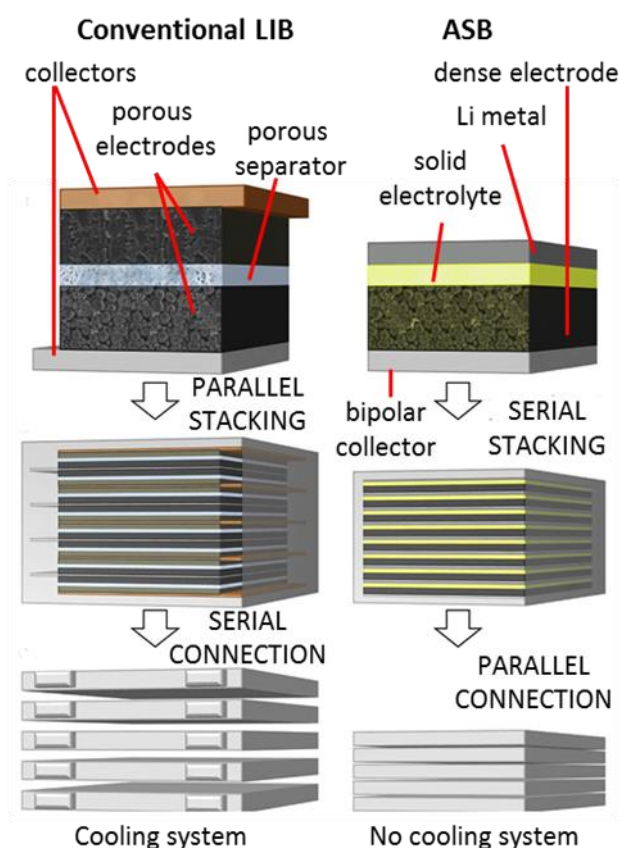*Corresponding author: claudio.gerbaldi@polito.it*

Figure 1. Comparison of battery pack assembly for conventional LIB and ASB. Reproduced, adapted and reprinted with permission from Ref 14.

Plastic crystals such as succinonitrile doped with lithium salts have also been considered as solid organic Li$^+$ conductive matrix and as additives to boost ionic conductivity in polymer electrolytes.[8,9] The major drawbacks of SPEs, mainly PEO-based SPEs, consist in low room temperature (RT) σ_i (below 10^{-4} S cm^{-1}) and low oxidative degradation potential (below 4 V vs Li$^+$/Li), preventing application with high voltage cathodes.[1,10] On the plus side, SPEs are generally low cost, lightweight, flexible, non-flammable and show improved compatibility with lithium metal as compared to LEs, enabling application in LMPBs.

Inorganic solid-state electrolytes (SIEs) are crystalline, glassy or glassy/ceramic materials[11] with excellent transport properties such as $t_{Li+} \approx 1$ and high (single-grain) σ_i, in some cases exceeding that of LEs which have gained them the designation of superionic conductors (by instance, in the case of thio-LISICON type Li$_{9.54}$Si$_{1.74}$P$_{1.44}$S$_{11.7}$Cl$_{0.3}$, LSPSC, RT σ_i = 25 mS cm^{-1}).[12] Ions that move in a crystalline SIE have to bypass bottleneck points, in practice energetic barriers between local minima along the diffusion pathways. To trigger the superionic conductivity, diffusion pathways with a low migration barrier, and a large number of crystallographic sites over which the moving ions can be distributed, are fundamental. The former properties are correlated with the anion sub-lattice and it has been shown that the body-centred cubic (bcc) anion packing offers a favourable energy landscape with very low Li$^+$ migration barrier (0.2 eV).[11] Glassy SIEs are generally synthesized by

rapid quenching of glass forming melts with high ionic conductivity and low activation energy for Li$^+$ ion conduction. The structure of glasses depends on that of the corresponding melts and, in general, the ionic conductivity of glassy SIEs is higher than that of the corresponding crystals. The addition of network modifiers and lithium salts as well as the mixture of glass formers with different anions have been experimented as viable strategies to improve the ionic conductivity of glassy SIEs. Highly conductive glass ceramic materials can be obtained by the partial crystallization of super Li$^+$ ion conductive crystalline phases from precursor glasses.[13]

The most studied SIEs consist in sulfide and oxide compounds. Some of them include expensive non-abundant elements such as Ge, like in the case of thio-LISICON type Li$_{10}$GeP$_2$S$_{12}$ (LGPS, RT σ_i = $1.2 \cdot 10^{-2}$ S cm^{-1}), making large-scale application unfeasible. Ge in LGPS is also responsible for its poor compatibility with Li metal. Among the oxides, those containing Ti^{4+}, such as perovskite-type Li$_{3x}$La$_{2/3-x}$TiO$_3$ (LLTO, RT $\sigma_i \approx 10^{-3}$ S cm^{-1}) and NASICON-type Li$_{1+x}$Al$_x$Ti$_{2-x}$(PO$_4$)$_3$ (LATP, RT $\sigma_i \approx 10^{-3}$ S cm^{-1}), can be reduced at the interface with metallic Li, turning into good electronic conductors. Sulfides are generally very sensitive to moisture, eventually resulting in H$_2$S evolution, implying expensive processing in inert atmosphere. Moreover, sulfides often display low oxidative degradation potential (~3 V vs. Li$^+$/Li).[1,11,14,15]

In recent years, composite (or hybrid) polymer electrolytes (CPEs) with SIEs as the filler have gain more and more attention, in an attempt to exploit the superior transport characteristics of the inorganic Li$^+$ conductors, while simplifying the preparation process, improving the interfacial contact with the electrodes and the ability to buffer the mechanical stress upon cycling. Excellent recent reviews on the properties and cell performances of CPEs are given by Keller et al.,[5] as well as other authors.[16,17] Ionic conductors used as fillers incorporated in SPEs can have a profound impact on the ion transport mechanism in polymers, in ways that are not fully understood yet. The formation of a percolation network through the inorganic phase depends upon the dimension, volume fraction, shape and orientation of the conductive filler. The organic/inorganic interface in CPEs has a great influence on the overall ionic conductivity. As is the case with composite polymer electrolytes encompassing inert non-conductive particles such as SiO$_2$ and Al$_2$O$_3$, Lewis acid-base interactions between the organic and the inorganic phase can affect the charge carriers mobility and salt dissociation. In CPEs with conductive inorganic fillers, the resistance to charge transfer across the two phases is affected by several factors, including Li$^+$ desolvation energy and the difference between Li$^+$ concentration and transference number in the two phases.[5,18] Polymer-particle composites not only can play a significant role in designing new electrolytes but are also expected to define new strategies for a better-controlled engineering of both the active cathode and anode materials and electrode microstructure, to generate advanced LIBs.

Table 1 Electrochemical performance and preparation process of all-solid lab scale cells from the reviewed literature.

Cell configuration	CE composition (ratio wt)	Discharge capacity & Capacity retention	T (°C)	Mass loading Thickness	CE Process & notes	Ref
Li/speXL/NMC	NMC/PEO-LiTFSI-PYR$_{14}$TFSI/KJ_c (43/60/7)	157 mAh g^{-1} (1st cycle , C/20) ≈ 66 % (100th cycle , C/10)	40	3-4 mg cm^{-2} 40-50 µm	-Dry blending of premixed AMPs - KJ_c with the polymer mixture -annealing 100°C -hot pressing 100°C -cold calendering	44
Li/speXL/LFP	LFP/P(EO)$_{10}$LiTFSI-(PYR$_{14}$TFSI)$_2$/KJ_c (43/60/7)	161 mAh g^{-1} (1st cycle, C/20) ≈ 100% (100th cycle, C/10)	40	4-5 mg cm^{-2} 40-50 µm	speXL = photo-crosslinked PEO-LiTFSI-PYR$_{14}$TFSI	
Li/PTEC-LiTFSI/LFMP	LFMP/Super P/PTEC/PVdF-HFP (80/10/6.7/3.3)	105 mAh g^{-1} (1st cycle, C/5) 100% (100th cycle, C/5)	55	1.3-1.8 mg cm^{-2}	-Cathode: Casting on Al -SPE: solvent (ACN) casting on cellulose nonwoven	79
Li/LPSC/c-NMC	NMC/LPSC/CB/EtC (15/3/2/0.2)	112 mAh g^{-1} (1st cycle, C/20) 90% (100th cycle, C/20)	30	≈ 4 mg cm^{-2}	Cathode: Dissolution (EtOH) -precipitation on Al -heat 80°C SE: cold press on Cathode	55
Li/LPSC/c-NMC	NMC/LPSC/CB (75/15/10)	45 mAh g^{-1} (1st cycle, C/20) 82% (100th cycle, C/20)	30		SE powder after 1 dissolution (EtOH) reprecipitation step	
Graphite/LSPC/LCO	LCO/PVdF/Super P (97/1/2) Graphite/PVdF (95/5)	117 (C/10), 75 (C/2) mAh/(g LCO) 96% (80th cycle, C/2)	30	LCO 10 mg cm^{-2} graphite 6 mg cm^{-2}	Cathode/anode: solvent (NMP) casting on collector -Dip-coating of the SE into the porous electrode by dissolution (EtOH)-reprecipitation -heat 180°C under vacuum -cold press @ 770 MPa SE pellet: heat treatment at 500°C	97
Li/LIM-LLZO/LCO	LCO/LIM/AB_c (50/40/10)	130 mAh g^{-1} (1st, C/10) 97% (150th cycle, C/10)	RT	LCO 15.9 mg cm^{-2} 139 µm	Cathode: cold press LIM-LLZO: cold press LIM-LLZO = mix of LIM (20%) and LLZO (80%) LIM = 1 g UIO-67 in 1.5 mL of LiTFSI in EMImTFSI	105

A relevant number of interfaces and interfacial regions are created especially when nanosized materials are introduced in electrochemical cells, thus opening up to some opportunities for enhanced electrochemical performances provided that the current manufacturing methods are updated.

Composite electrodes (CEs) for currently available LIBs with liquid electrolytes consist of an electrochemically active material, a binder (usually a non-conducting polymer, such as PVdF or CMC), a conductivity enhancer, and interconnected porosity to let the LE permeate the electrodes. Homogeneous electrode porosity is pivotal to improve battery performance, as it promotes faster Li$^+$ diffusion and mitigates surface solid electrolyte interphase losses by passivation. An optimal electrode chemistry and architecture permits maximum electrolyte access, facilitates charge transfer and ionic diffusion, provides continuous electron pathways through effective dispersion of additives, and accommodates volume expansion.

In conventional batteries, porous electrodes are wet by the LEs enabling ion conduction, whereas in ASBs ion conduction is limited to the contact area between the solid electrolyte and the active material particles (AMPs) (see the section on Interfacial compatibility).[19]

Therefore, SIE should be loaded into composite electrodes, thus decreasing the active material fraction. In addition, the density of solid electrolytes is higher than that of liquids and polymers used in common batteries, and a higher amount of solid is required to ensure homogeneity and continuous ionic pathways, which is detrimental for improving the energy density of ASBs. Possible solutions include surface coating the AMPs with the solid electrolyte, homogeneous embedding in SLICs or SPEs, with electronic wiring provided by carbon additives[15] or electroactive polymers.[20]

Ensuring an optimal contact at the electrode/electrolyte interface and unravelling the reactions occurring therein, represents major challenges in the field of ASBs.[14,21]

As compared to systems with binary LEs, CEs with single ion conductor solid electrolytes, such as SIEs and single Li$^+$ ion conductors (SLICs), are, in principle, able to deliver larger specific capacity at higher current densities despite a lower conductivity or a higher thickness.[22] Nevertheless, there are only spare reports of high power ASBs outperforming common LIBs with LEs.[12] Achieving high energy density implying high mass loading is still a challenging task with solid electrolytes, closely tied to the preparation process, even with highly conductive sulfide SIEs.[21] Once the preparation process is optimised, the electrode/electrolyte stacking requires a lower amount of internal connections in the final device as compared to assembly with LEs, resulting in a further improvement of energy density (*Figure 1*).[14]

The investigations on ASBs are rapidly progressing and significant breakthroughs in the performance are periodically announced. Although several reviews have summarized the preparations and main characteristics of solid electrolytes for LIBs it is believed that a review covering the specific issues concerning the charge transport properties inside the CEs (for both all inorganic and hybrid systems) and providing an insight into the critical aspects of CEs affecting cell operation and their characterisation is still needed. In order to give a better picture of the current state-of-the-art in the field and promote a targeted research towards the design of optimal interfaces possessing improved transport properties, this review aims to collect recent, fundamental works focused on the preparation methods of CEs, the effect of their composition and morphology on the cell performance, and electrochemical impedance spectroscopy and other techniques that have been employed to reach a deeper knowledge of the transport characteristic of Li$^+$ in solid composite electrolytes and electrodes.

In this review, the first section will introduce CEs features and some experimental methods to investigate ionic conductivity and tortuosity. This is followed by an overview of the fabrication methods and current cell chemistries to aid the understanding of the performance-affecting factors in the design and optimization of CEs and ASBs. The preparation processes and performances of representative cell chemistries are summarised in Table 1 and a more comprehensive list is given in Table S1 (Supporting Information) to provide the reader with important information about the compositions of CEs, that not always are clearly reported (see also comments by Passerini and co-workers[5] about this). Then, the interfacial contact and chemistry at the interfaces between active and inactive components is also discussed. Finally, the major challenges and perspectives are documented and possible research directions in overcoming the challenges are proposed.

2 CEs

The experimental techniques and models useful to understand the impact of CEs on the cell performance address the components and characteristics of the system as well as the failure mechanism.

This section is focused on the electrochemical measurements commonly used to evaluate the influence of the starting materials, formulation and preparation processes on the transport properties and the microstructure of the CEs, and on the electro-chemo mechanical stress.

An overview of the most advanced techniques (*in-situ*, *in-operando*, and *post-mortem* analysis) with attention to those used to evaluate the failure mechanism is offered by Ma et al.[27]

2.1 Composition and material characteristics

An electrode in a common LIB is essentially a four-part composite system comprising the electrochemically active material, a binder, a conductivity enhancer, and interconnected porosity. The geometric considerations of the electrode design have been shown to be critical in how they influence heterogeneous transport processes and concentration gradients that will affect a battery operation; the available surface area per unit volume influences the reactivity of the active material.
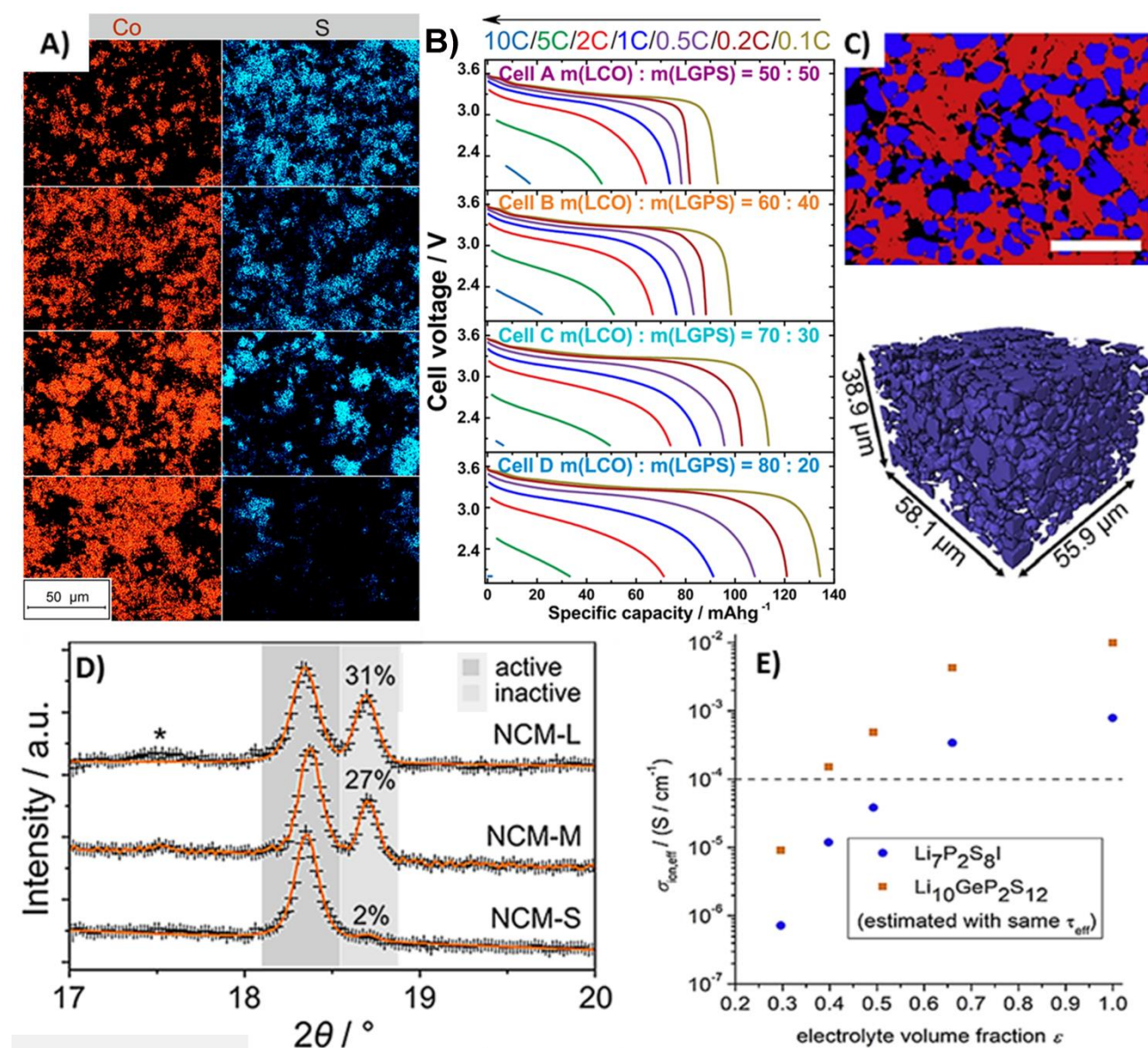
Figure 2. A) EDX mapping of CEs and B) discharge curves of Li-In/LGPS/LCO cells with different mass ratios ranging from 50 to 80 % wt of LCO. Reproduced, adapted and reprinted with permission from Ref 29. C) Reconstruction of a LPS-LCO CE from FIB-SEM tomography. Reproduced, adapted and reprinted with permission from Ref 31. D) Rietveld plots of the 003 reflection of NMC622 from ex-situ XRD analysis of charged NMC/LGPS CEs with large (NMC-L), medium (NMC-M) and small (NMC-S) AMPs. Reproduced, adapted and reprinted with permission from Ref 25. E) Plot of $\sigma_{i,composite}$ versus the volume fraction of SIE in a LPSI-LTO-C_{65} CE. Reproduced, adapted and reprinted with permission from Ref 32.

LIBs are sensitive to the available surface area density within the electrode, and so the effects of particle morphology and electrode porosity are inter-related and need to be considered together. A fundamental parameter affecting Li^+ and electron pathways through CEs is the residual porosity. The hindrance of Li^+ transport due to an interconnected network of non-conductive phases (such as pores) can be denoted as tortuosity (τ), even though this term can be ambiguous, because it is also used to define the ratio between the effective path length and the domain thickness for a diffusing species.[23] The value of τ is strongly related to the microstructure. This tortuosity is often anisotropic and can lead to high macroscopic ohmic resistance, which will hamper the delivered energy and power density of the battery.

The microstructure of CEs in ASBs is affected by several factors, including particle dimensions, adhesion and voids (linked to the material characteristics and preparation method), as well as composition and thickness. These parameters ultimately affect the electronic and the ionic pathways within the composite electrodes. In this section, some examples of recent investigations including advanced experimental and simulation techniques are given on how the CE composition and materials characteristics (e.g., particle size) in CEs affect the microstructure, the transport properties and the overall cell performance.

CEs consisting of SIEs and sufficient AMPs for application can have 10–20% porosity, resulting in a discontinuous pathway for Li⁺ ions. Zhang et al.[24] investigated the effect of AMP/SIE mass fraction (from 40/60 to 80/20, corresponding to LCO loading from ≈ 5 to 10 mg cm⁻²) in CEs consisting of LCO (LiNb$_{0.5}$Tb$_{0.5}$O coated) and LGPS on the rate performance of Li-In/LGPS/LCO cells obtained by uniaxial cold pressing. The area and the overall mass of the CE and the solid electrolyte separator were kept constant in all cases, resulting in a thickness of ≈ 90 μm for all the samples. No electron conductive additives were used in this experiment to avoid side reactions. Under this condition, below 50 % wt of LCO it was not possible to obtain good electrochemical performances because of low σ_e due to insufficient contact among the AMPs. This fact was confirmed by energy-dispersive X-ray (EDX) spectroscopic mapping of Co, coupled with SEM analysis of the CEs (*Figure 2*A). Overall, it has been found that ionic percolation pathways are more important to achieve high rate capability (and ultimately power density) whereas, for high energy ASBs, the electronic percolation appeared to be the crucial factor (*Figure 2*B). Under the experimental conditions adopted, 20 % wt of SE in the CE has been enough to achieve good specific capacity values at low current densities (below 2C, i.e. ≈ 2.8 mA cm⁻² with 80 % wt of LCO).

Besides the aforementioned indirect effect on electronic percolation, the AMP size plays a fundamental role in the cell performance. An example is given in a recent work about the effect of NMC particles size on the performance of lab-scale cells in the configuration In/Li$_3$PS$_4$/NMC622 (60% Ni) and obtained by cold pressing.[25] The activity of NMC particles is investigated by combining galvanostatic cycling and *ex-situ* XRD analysis performed on the CEs dismounted from the cell after charging (delithiation). The XRD analysis is based on the splitting of the 003 reflection of the layered oxide structure (space group R3̄m h) arising from NMC species with a different Li content after delithiation upon charging (at 25 °C and C/10 rate being 1C = 180 mA g⁻¹), which are quantified by means of Rietveld refinement analysis (*Figure 2*D). By comparison with the parameters extracted from operando XRD upon cycling using a reference liquid cell, it has been therefore possible to assess the effective activity and SOC of the AMPs, notwithstanding possible side reactions. The CE consists of Li$_3$PS$_4$ and NMC622 (30:70 % wt), with pristine uncoated NMC particles and without any carbon additive to avoid detrimental reactions with the SIE. The fraction of inactive AMPs is found to range from 2 (small particles 4-5 ≈ μm) to 31 % (large particles 20 ≈ μm). AC/DC measurements of conductivity evidence that σ_e is strongly influenced by the particle size, decreasing by three orders of magnitude passing from small to large particles, due to the lack of sufficient interconnection between large particles. In this regard, polymer electrolytes offer several advantages over SIEs, because of better adhesion to the AMPs and the easier, scalable processes required to obtain homogeneous and thin SPE and CE films. By instance, cold calendering after hot-extrusion of aforementioned CEs containing a PEO-based electrolyte, LMO and Super C$_{65}$ resulted in 100 μm thick films with negligible porosity within the experimental error of picnometric density measurements. These results have been obtained regardless the SPE mass fraction,

being the amount of PEO-based electrolyte in the range 30 - 35 %. wt, which is comparable to that of LPSI in the CEs in the aforementioned studies.[26] Based on density, LMO mass fraction and film thickness, LMO loading in these films is ≈15 mg cm⁻².

Appetecchi et al.[26] used EIS to investigate the effect of solid electrolyte mass fraction in CEs based on PEO electrolytes with LiCF$_3$SO$_3$ (EO/Li = 20/1) obtained by hot-extrusion and subsequent cold calendering. Two series of samples are obtained, consisting of varying amounts of SP_c and the PEO electrolyte (series I) or LiMn$_2$O$_4$ (LMO), carbon and the PEO electrolyte (series II). LMO content is varied from 60 to 58.5 % wt, and it is worth mentioning here that LMO is a cathode material with poor σ_e. In symmetric cells with ion blocking electrodes at 20 °C, the films acted as simple resistors at carbon content ≥ 5 % wt (i.e., 3.1 % in terms of volume), resulting in a point on the real-axis in the Nyquist plot. This indicates the presence of a continuous highly conductive electron pathway through the film. For the series II films, the impedance spectra resulted in a point on the real-axis at carbon content ≥ 6 % wt (i.e., 6.6 % in terms of volume). Overall, considering the volumetric fractions of the components in samples from series I, it has been found that ≈ 3 % vol of carbon NPs (≈ 30 nm) is required to achieve a continuous percolation pathway through the semi-crystalline PEO electrolyte at 20 °C. In series II, due to the hindrance of large LMO particles (≈ 10-35 μm), electron percolation is achieved for a double volumetric fraction of carbon ≈ 7 % vol.

2.2 Conductivity in SEs

This paragraph is aimed to give a very short, basic introduction of the main theoretical concepts on ionic conduction since many excellent fundamental works provide details on this topic and on the theory of conduction in composite materials (see for example the work by Maier et al.[28]) that are beyond the scope of this present article.

All solid materials can experience two types of conductivity, namely electronic and ionic. Although of high interest σ_e has been less investigated than σ_i in LIBs. The electronic conductivity is related to the transfer of electrons and ideally should be higher than 1 S cm⁻¹ to assure fast charge and discharge. Solid electrolyte separators must have negligible electronic conductivity to avoid short circuits. In CEs, electronic percolation is generally ensured by the addition of conductivity enhancers such as carbons in various forms (e.g., carbon black).

The general model of ionic conductivity that can explain the properties of both polymers and SIEs is the Arrhenius model, is expressed by:[10]

$$\text{Equation 1} \qquad \sigma_i = \frac{\sigma_0}{T} e^{-E_A/k_B T}$$

where E_A is the activation energy related to the migration of the ions, T is the temperature in Kelvin, k_B is the Boltzmann constant and σ_0 is the pre-exponential factor which contains the entropy of the migration and the charge carriers. High conductivities are achieved when the activation energy is low and the concentration of mobile ion carriers is high.

Other models were developed to describe the behaviour of SPEs such as the Vogel-Tammann-Fulcher which can explain the non-linear

logσ$_i$ *vs* 1/T graphs taking into account the ion transport in amorphous polymers through the continuous motion and relaxation of the polymer backbone. The factors affecting ion transport in SPEs and in SIEs are thus related to the fraction of mobile ions n_i, ionic mobilities u_i and ionic charges q_i but also to the intrinsic characteristics of the materials, according with the following equation:[10]

$$\text{Equation 2} \qquad \sigma_i(T) = \sum_i n_i\, q_i\, u_i$$

The ionic conductivity of a SE can be readily determined by EIS spectroscopy using symmetric cells with ion blocking electrodes (e.g., in the SS/SIE/SS or SS/SPE/SS configuration, where SS = stainless steel).The equivalent circuit for this configuration consists in the parallel combination of the geometric capacitance and a series connecting the bulk resistance (R_{bulk}) with the double layer capacitance. The ionic conductivity is given by:[10]

$$\text{Equation 3} \qquad \sigma_i = \frac{d}{R_{bulk}\, A}$$

Where *d* and *A* stand for the electrolyte thickness and the electrode area, respectively.

2.2.1 Methods to determine conductivity in CEs

The most common protocol used to determine both σ$_i$ and σ$_e$ in a CE is based on EIS and the direct current (DC) polarisation (AC/DC polarisation) using symmetric cells under ion blocking condition (e.g., in the SS/CE/SS configuration). With this setup, EIS yields both σ$_i$ and σ$_e$, whereas the DC method allows determining σ$_e$. The value of σ$_i$ can also be determined by the DC polarisation method, but symmetric cells under electron blocking conditions (such as SS/SE/CE/SE/SS) are required. DC polarisation can be performed in either galvanostatic[29] or potentiostatic[30] mode. For what concerns the application to CEs with solid electrolytes, Asano et al.[30] have recently determined σ$_i$ and σ$_e$ in NMC-Li$_3$PS$_4$ (varying NMC content from 48 to 62 % vol) CEs by all the aforementioned methods. The potentiostatic DC polarisation is performed at 0 and 50 % SOC. A constant voltage of 50 mV is applied in order to measure the steady state current. The discrepancy between the results yielded by the different techniques adopted are higher for σ$_i$ (20 %) than for σ$_e$ (5 %). The expected increase of σ$_e$ with increasing the SOC of LCO is clearly observed, whereas the changes in σ$_i$ are negligible. The electrochemical performance of the CEs has been also tested in In-Li/LPS/NMC cells. In agreement with the previously mentioned results from Zhang et al.,[24] at high NMC contents in the CE (i.e., higher σ$_e$) the delivered discharge capacity is low at high current density, meaning that σ$_i$ is the limiting factor for high power application. Another recent article[29] reported about the transport properties of LCO-LLZO (Al-doped) CEs obtained by warm-press (250 °C) and subsequent annealing at 700 °C. CEs with different weight ratios of LCO to LLZO were prepared and tested, namely 3:1, 1:1 and 1:3. The value of σ$_e$ was determined by either EIS analysis or DC polarisation of Au/CE/Au cells. In this case, DC polarisation was performed in the galvanostatic mode. Both methods yielded similar values for σ$_e$, which is the predominant contribution in the

impedance spectrum. Indeed, the values of D$_{Li+,composite}$ and σ$_{i,composite}$ were extracted by DC galvanostatic polarisation under electron blocking condition in Li-Al/LiI/CE/LiI/Li-Al cells, where Li-Al alloy and LiI were used as the current collector and the electron blocking layer, respectively. The value of σ$_e$ was found to be dependent on the fraction of the electron conductive phase, whereas the value of σ$_{i,composite}$ was found to be 7 orders of magnitude lower than σ$_i$ of the pure LLZO phase, irrespective of LCO fraction. The microstructural analysis by FIB-SEM tomography reveal that LLZO domains (≈2.5 μm) were isolated by larger LCO clusters (≥2.9 μm), hindering ion diffusion.

Such phenomenon was not reported for CEs with sulfide SIEs obtained by cold pressing. Tuning the pores as well as the size and distribution of particles is thus envisaged as a possible solution.

2.3 EIS Models for the investigation of transport properties

In this section, the conditions and the equivalent circuits used to extract the main transport properties in CEs are summarised.

2.3.1 Electron blocking condition. This condition is met with cells like Li/SE/CE/SE/Li, SS/SE/CE/SE/SS etc. where the solid electrolyte works as the electron blocking layer (*Figure 3*).[31,32]

Assuming that the interfaces between the layers inside of the cell give no contribution, the high frequency signal is given by:

$$\text{Equation 4)} \qquad Z_{high\ frequency} = 2R_{bulk} + \frac{R_{ion}R_e}{R_{ion}+R_e}$$

where R$_{bulk}$, R$_{ion}$ and R$_e$ are the electrolyte bulk, ion diffusion and electron diffusion resistances, respectively.

As there are two SE layers, the value of R$_{bulk}$ is multiplied by 2. If the σ$_e$ value is high (as in the case of delithiated LCO used by Hlushkou et al.[31]), the high frequency impedance is given by:
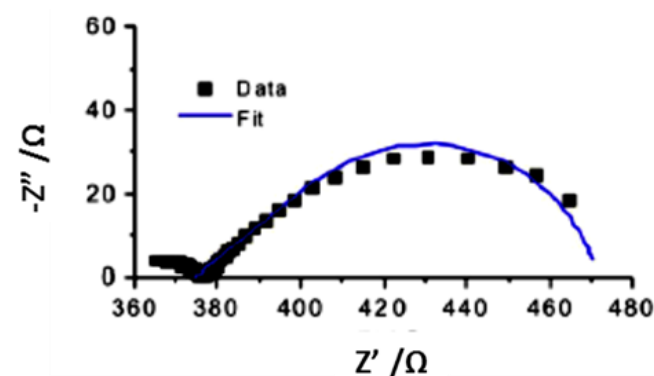

Figure 3. Nyquist plot of Li/SE/CE/SE/Li cell with high σ$_e$. The SE is LPSI and the CE consists of LPSI and delithiated LCO. Reproduced, adapted and reprinted with permission from Ref 32.

$$\text{Equation 5)} \qquad Z_{high\ frequency} = 2R_{bulk}$$

At low frequency, the signal only depends upon ion diffusion:

Equation 6) $\qquad Z_{low\ frequency} = \frac{R_{ion}}{(i\omega\beta)^\alpha} tanh(i\omega\beta)^\alpha$

where β is the ion diffusion time constant and α is usually set at 0.5 (ideal case). The total impedance is given by:

Equation 7) $\qquad Z_{total} = Z_{high\ frequency} + Z_{low\ frequency}$

2.3.2 Transmission line model (TLM) with no faradaic reactions. In this case, the SE is in direct contact with the electron conductive electrodes, in cell configurations such as SS/CE/SE/CE/SS.[32,33] The TLM models the processes occurring in cylindrical pores of radius r and length corresponding to the CE thickness $d_{composite}$.

The equivalent circuit is built using the resistances per unit length (Ω cm) to ion (r_{ion}) or electron (r_e) diffusion. Different TLM can be used, depending on σ_e. The equivalent circuit and the resulting typical impedance spectra in the case of high or low σ_e are given in *Figure* 4A,C and *Figure* 4B,D, respectively.

For the high σ_e case, the impedance of the TLM is given by (*Figure* 4A,C):[32]

Equation 8) $\qquad Z_{TLM} = R_{bulk} + \sqrt{\frac{R_{ion}}{i\omega C_{dl}}} coth\sqrt{R_{ion}i\omega C_{dl}}$

where C_{dl} is the total double layer capacitance at the interface between the SE and the active material.

Kaiser et al.[32] extracted the total R_{ion} and C_{dl} from the circuit elements per unit length r_{ion} and c_{dl} as follows:

Equation 9) $\qquad R_{ion} = \frac{d_{composite}\ r_{ion}\ \pi\ r^2}{A_{composite}\ \varepsilon}$

Equation 10) $\qquad C_{dl} = \frac{c_{dl}\ d_{composite}\ A_{composite}\ \varepsilon}{r}$

where $A_{composite}$ and ε are the area of the CE and the volume fraction of the solid electrolyte, respectively.
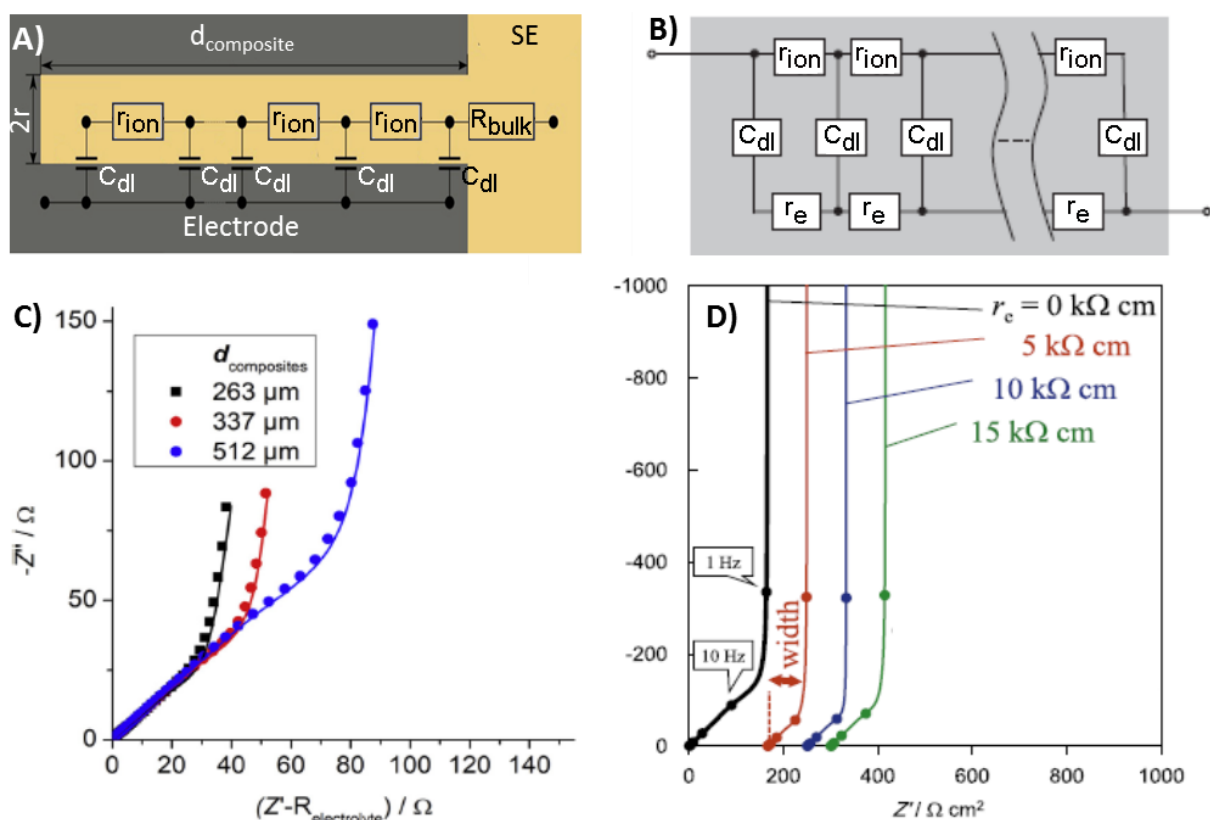

Figure 4. TLM equivalent circuit for SS/CE/SE/CE/SS cells in the case of high[32] (A) and low[33] (B) σ_e. Simulation of the impedance spectra resulting from the TLM for high[32] (C) and low[33] (D) σ_e. Reproduced, adapted and reprinted with permission from Ref 32 and 33.

For the low σ_e case, the impedance of the TLM is given by (*Figure* 4B,D):[33]

Equation 11)
$$Z_{TLM} = \frac{r_{ion}r_e}{r_{ion}+r_e}d_{composite} +$$
$$\frac{(i\omega c_{dl})^{-0.5}}{(r_{ion}+r_e)^{3/2}} \frac{(r_{ion}{}^2+r_e{}^2)\cosh d_{composite}\sqrt{(r_{ion}+r_e)\,i\omega c_{dl}}+2\,r_{ion}r_e}{\sinh d_{composite}\sqrt{(r_{ion}+r_e)\,i\omega c_{dl}}}$$

Differently from the previous case, the high frequency intercept on the real axis is not zero when $r_e \neq 0$ (*Figure 4*D), and it is given by:

Equation 12) $Z_{\omega \to \infty} = \frac{r_{ion}r_e}{r_{ion}+r_e}d_{composite}$

The real part of the portion of the spectrum denoted as "width" in *Figure 4*D corresponds to:

Equation 13) $Z_{width} = \frac{1}{3}(r_{ion}+r_e)\,d_{composite}$

An interesting adaptation of the TLM model for materials with relatively low σ_e led to the equivalent circuits shown in *Figure 4*B and 5A. A ladder network with multiple rows was developed where each of the rows includes infinitesimal elements representing the ionic resistance, the interfacial impedance (per unit volume) and the electronic resistance.

2.3.3. Ion blocking condition. This condition is met with cells in configuration such as SS/CE/SS, with the CE in direct contact with ion blocking electrodes. In the absence of charge transfer at the interface between the active material and the solid electrolyte, the theoretical value of the total impedance (equivalent circuit in *Figure 5A*) is given by:

Equation 14) $Z_{total} = \frac{r_{ion}r_e}{r_{ion}+r_e}d_{composite} +$
$$\frac{2r_e{}^2(i\omega c_{dl})^{-0.5}}{(r_{ion}+r_e)^{3/2}} \frac{\cosh d_{composite}\sqrt{(r_{ion}+r_e)\,i\omega c_{dl}}-1}{\sinh d_{composite}\sqrt{(r_{ion}+r_e)\,i\omega c_{dl}}}$$

Here it is worth noting that the equivalent circuit in *Figure* 5A differs from that of *Figure* 4B for the connections to the circuit terminals, which reflect the different conditions (*Figure* 4B corresponds to a TLM with no faradaic reactions and low σ_e, which is different from the ion-blocking condition described by the circuit in *Figure* 5A). The Nyquist plot resulting from the circuit in *Figure* 5A consists in a 45°

feature closing as a semicircle, as shown in *Figure 5B*. In the absence of additional low frequency signals, electron conductivity is predominant. Therefore, denoting Z' the impedance of the signal in *Figure 5B*, the high and low frequency intercepts on the real axis are given by:

Equation 15) $Z'_{\omega \to \infty} = \frac{r_{ion}r_e}{r_{ion}+r_e}d_{composite}$

Equation 16) $Z'_{\omega \to 0} = r_e d_{composite}$

In addition to Z', a small semicircle at high frequency has been observed, possibly arising from capacitive elements in parallel with either r_{ion} or r_e (*Figure 5C*).[30,33]

2.4 Estimation of tortuosity

Experimental methods such as EIS and simulations based on 3D reconstruction of the CE microstructure from tomography data have been recently used to estimate tortuosity in CEs (*Figure 2C*).[31]

The value of τ in composite electrodes can be defined as the ratio between the electrolyte σ_i (extracted from the impedance of the solid electrolyte under ion blocking condition) weighted by its volume fraction (ϵ) in the composite and the ionic conductivity of the composite ($\sigma_{i,composite}$). Similarly, τ can be computed knowing the diffusion coefficient of Li$^+$ in the electrolyte (D_{Li+}) and in the composite electrode ($D_{Li+, composite}$):

Equation 17) $\tau = \frac{\epsilon \cdot \sigma_i}{\sigma_{i,composite}} = \frac{\epsilon \cdot D_{Li+}}{D_{Li+,composite}} = \frac{D_{Li+}}{D_{Li+,effective}}$

The value of $\sigma_{i,composite}$ can be extracted from the resistance to Li$^+$ ion transport (R_{Li+}) through the solid electrolyte in the CE. If the solid electrolyte is not a SLIC (as in the case of SPEs with a dissolved Li salt), some adjustments would be required, in order to include t_{Li+}. The value of R_{Li+} can be extracted from EIS (see above for a more detailed discussion).
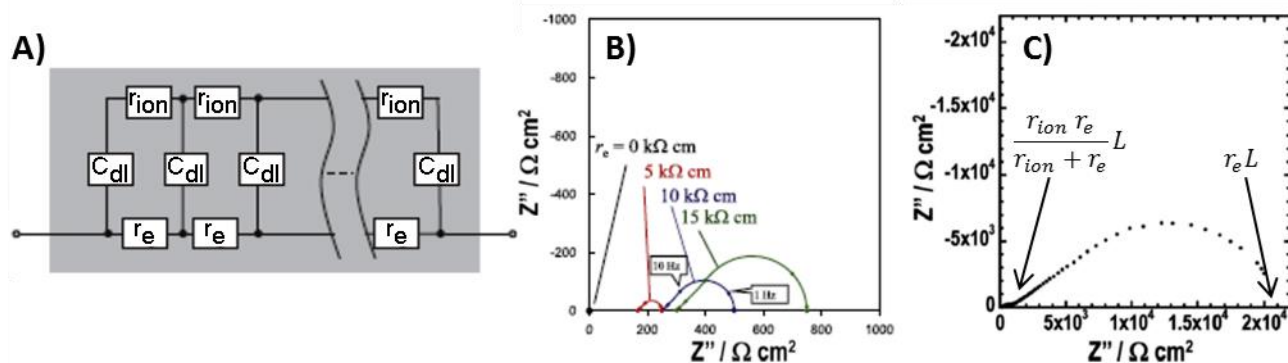

Figure 5. A) Equivalent circuit for symmetric cells with ion blocking electrodes (e.g., SS/CE/SS). B) Simulation of the impedance spectra for different values of r_{ion} and r_e. C) Nyquist plot of a SS/CE/SS for a CE consisting of NMC (48 % vol) and Li$_3$PS$_4$ (52 % vol) (here L stands for $d_{composite}$). Reproduced, adapted and reprinted with permission from Ref 30 and 33.

Hlushkou et al.[31] studied the impact of τ on the transport properties of a CE consisting of LPS/LiI (LPSI, 67:33 wt %, RT σ_i = 0.7 mS cm^{-1}) glassy SIE and LiNbO$_3$ coated LCO (LCO/SIE, 59:41 % wt, 38:62 % vol). The CEs were previously delithiated upon charge in Li$_4$Ti$_5$O$_{12}$/SE/LCO cells, and then recovered to perform the EIS measurements. Under this condition, LCO is an excellent electron conductor.[34] The value of τ from EIS was compared to that obtained by feeding a simulation for ion transport with data resulting from a morphology reconstruction based on focused ion-beam scanning electron microscopy (FIB-SEM) tomography. The value of $D_{Li+,effective}$ (see Equation 17) was extracted from the simulation using a random walk particle tracking approach, in which particles displacement results from the combination of stochastic processes and diffusion laws. The same procedure was adopted to compute τ in a virtual CE with zero porosity, where the voids from the morphology reconstruction are filled with the SIE. Overall, the values of τ from EIS, the reconstructed CE and the virtual void-free CE were found to be 1.6 ± 0.1, 1.74 and 1.27, respectively. The porosity of the CE is found to be ≈ 13 %, which has been enough to lower the simulated value of $D_{Li+,effective}$ by 37% with respect to the virtual zero-void CE, confirming the importance of suppressing porosity.

Kaiser et al.[32] used an approach similar to that used by Hlushkou et al.[31] for the determination of τ from EIS measurements, in order to investigate composite anodes comprising Li$_4$Ti$_5$O$_{12}$ (LTO), C$_{65}$ carbon and LPSI with different volume fraction of LTO and SIE. The value of R_{Li+} was extracted from fitting of the impedance spectra of either Li/SE/CE/SE/Li (i.e., electron blocking) or SS/CE/SE/CE/SS. In the former case, the cell configuration was similar to that used by Hlushkou et al.[31] In the latter case, the experimental data were fitted to a transmission line model (TLM) assuming no faradaic processes and low resistance to electron diffusion (R$_e$). A remarkable decrease of $\sigma_{i,composite}$ was observed with reducing ε, due the increased τ at lower SE content (*Figure 2*E). The TLM approach yielded to unreliable values for τ at low ε (below 40 % vol, i.e. ≈ 32 % wt), due to the basic TLM assumption that Li$^+$ ion pathway in the solid electrolyte is homogeneous throughout cylindrical pores. Based on the estimated value of 0.6 mS cm^{-1} for Li$^+$ conductivity (devoid of the anion contribution) in LEs with dissolved LiPF$_6$, it was inferred that single ion conducting solid electrolytes with ε = 0.4 in the CE should have σ$_i$ ≥ 5 mS cm^{-1} to be competitive with currently available Li-ion batteries in terms of power density. Despite SIEs with such σ$_i$, are known, it is fundamental optimising the preparation process so as to decrease the volume fraction of the solid electrolyte while keeping a low porosity, in order to overcome LEs.

Finally, it is worth mentioning the investigation carried out by Kato et al.,[35] who studied the effect of the CE thickness using different sulfide SIEs (LGPS, LPS and LPSI) in lab scale graphite/SIE/LCO cells obtained by cold pressing. The LCO loading was varied along with the thickness, differently from Zhang et al.[24] who varied the AMPs loading in ≈90 μm thick electrodes. The composite cathodes prepared by Kato et al. consisted of the SIE, LiNbO$_3$ coated LCO and AB_c, whereas the composite anodes consisted of the SIE and graphite. The thickness of the CEs was varied from 75 to 600 μm, with cathode limited areal specific capacity increasing from 2.0 to 15.7

mAh cm^{-2} (LCO loading from 14.5 to 115.4 mg cm^{-2}) along with the thickness. The performances were evaluated by EIS and galvanostatic cycling at different current densities. At low current densities, all the cells displayed good electrochemical performances. At higher rates, the decay of the areal discharge capacity was found to be dependent on the current density and the SIE conductivity rather than the thickness. The results were interpreted on the basis of the reaction zone model, assuming that the evolution of the ohmic potential drop upon discharge was dependent on $\sigma_{i,composite}$, and therefore σ$_i$, ε and τ. The effect of σ$_e$ wais not considered as a limiting factor. The estimated τ for the systems under examination was higher for the anode (3.32) than for the cathode composites (2.47). Overall, it was estimated that SIEs with σ$_i$ ≥ 10 mS cm^{-1} would enable 600 μm thick electrodes to deliver the full capacity at 30 mA cm^{-2}. Moreover, a doubling of the capacity delivered at 20 mA cm^{-2} with LGPS was envisaged by removing voids, that is decreasing τ to its minimum value by the optimisation of the preparation process. For what concerns the cycle life, pressure control was mentioned as a possible necessary measure.

2.5 Simulation of the cycling behaviour taking into account the microstructure parameters

As mentioned in the previous section, the influence of the CE microstructure on transport properties is quantified as τ, and it can be accounted for in modelling the cycling behaviour. The parameter τ for a sample with one conductive and one insulating phase can be given as a function of the volume fraction of the conducting phase according to the Bruggeman relationship:[36]

Equation 18) $$\tau_{Bruggeman} = \varepsilon^{-\alpha}$$

where α = 0.5 for spherical non-conducting particles.

Hlushkou et al.[31] found good agreement between $\tau_{Bruggeman}$ and the value of τ estimated from $D_{Li+,effective}$ (see Equation 17) for an ideal virtual CE with zero porosity. In the case of a real samples with voids, $\tau_{Bruggeman}$ was found to be underestimated as compared to the value of τ extracted from EIS.[31,32]

The value of α has also been altered in order to give a better estimation of tortuosity in porous electrodes for batteries. By instance, Braun et al.[37] calculated $\tau_{Bruggeman}$ with α = 0.9 as one of the microstructure parameters for a 1D homogenised model to simulate discharge profile of ASBs. The other microstructure parameters were ε (for the solid electrolyte) and the AMPs size. Geometry, mass and temperature were also considered. For what concerns electrochemistry, the charge transfer resistance and the corresponding time constant for both the anode and the cathode were extracted from impedance spectra of LTO/LGPS/LCO cells at different states of charge. In this case, the equivalent circuit model consisted in a series of 30 RC circuits and a capacitor. Each RC circuit is a parallel combination of a resistor and a capacitor. This method has been used in the place of the exact equivalent circuit based on the TLM, in order to obtain proper electrochemical parameters for the computation of the time-dependent overpotential. The high frequency resistance R$_0$, which is mainly due to R$_b$, was also extracted from impedance. The proposed model allows modelling the cell

behaviour with a limited number of parameters. Anyway, this kind of approximation led to significant differences (> 10 %) between the simulated and the experimental curves at high C rates (> 7.2 C) because the latter are diffusion controlled, whereas the model can properly describe a system in equilibrium state.

Differently, as mentioned before, Kato et al.[35] extrapolated τ from the analysis of the discharge behaviour of lab-scale LTO/LGPS/LCO cells based on the so called reaction zone model. As the potential drop at the end of the discharge curve was considered to depend on the ionic conductivity (i.e., the electronic conductivity was not considered as a limiting factor), the discharge capacity *C* at the ohmic limit considering the cut-off voltage (V_{cutoff}) was modelled as:

Equation 19)
$$C = t_d i = \frac{1}{i}\left(\frac{1}{q_c \sigma_{i,composite\ c}} + \frac{1}{q_a \sigma_{i,composite\ a}}\right)^{-1}\left(U_c^\theta - U_a^\theta - V_{cutoff} - R_0 i\right)$$

where U^θ is the open circuit potential of the active material, *q* is the capacity density of the CE and t_d is the time at which the cell reaches V_{cutoff}. The subscripts *a* and *c* stand for anode and cathode, respectively.

The experimental discharge capacity values from the rate capability tests were plotted versus the imposed current and data were fitted according to Equation 19 so as to extract the $\sigma_{i,composite}$ being all the other parameters known. This model could help understanding the limits of solid electrolyte materials with high diffusivity when high AMPs loading are used and estimating the foreseen improvement of the cell performance over reducing τ.

Alternatively, a microstructure-resolved approach can be used for simulations, so that the geometry, composition and microstructure of the cell components can inherently be taken into account. Recently, this method has been applied to simulate the cycling behaviour of a Li/LLZO/LCO cell in a virtual 3D reconstruction based on FIB-SEM tomography (*Figure 6*).[38] The microstructure resolved model was validated by comparison with the experimental data at different temperatures. The system contained uncoated LCO and Ta-doped LLZO in both the solid electrolyte and the CE. The simulation was fed with information from direct measurements (the solid electrolyte σ_i, thickness and Li+ concentration based on LLZO formula and the sample density) and literature (σ_e, Li+ diffusion coefficient, OCV, exchange current and theoretical capacity for LCO). In the modelled cell, the CE was based on the reconstruction of a portion of the real composite layer. As the region chosen for building the simulation was more homogeneous than the rest of the CE, the computed discharge capacity was overestimated as compared to the real one. Anyway, the voltage profile was accurately reproduced at 100 °C.
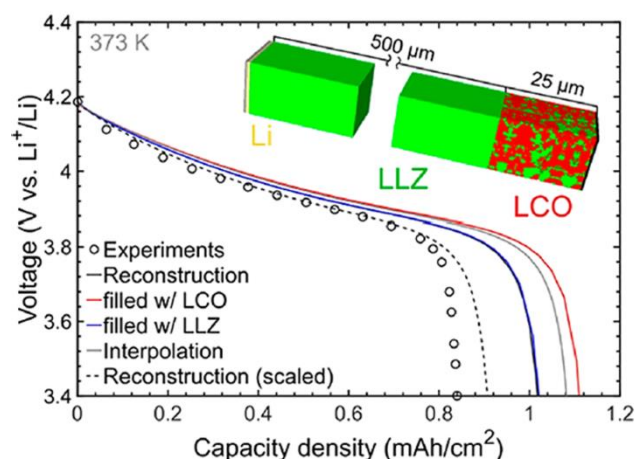

Figure 6. Simulated Li/LLZO/LCO cell based on a 3D reconstruction derived from FIB-SEM tomography (Inset). Discharge curves at 100 °C from experimental measurement (open circles) and from simulated data for as reconstructed (black) and void-filled mixed cathode (red = LCO, gray = mixed, blue = LLZ). Reproduced, adapted and reprinted with permission from Ref 38.

At RT, the real cell performance was remarkably poor, whereas, according to the simulation, the electrochemical performances at 100 °C and RT were similar, with an estimated ohmic loss of 9 mV caused by the decrease of σi with the temperature. This mismatch was explained in terms of polarisation effects due to the formation of interlayers because of side reactions at the AMPs/LLZO interface, which were not considered in the model.

2.6 Electro-chemo mechanical stress.

Many of the works mentioned so far highlight the importance of optimising the CE preparation process in order to decrease the amount of solid electrolyte and consequently to increase the energy density and obtain a homogeneous system with highly conductive ionic pathways without voids.

In any case, ASBs experience mechanical stress during operation because of the volumetric changes of the AMPs upon charge/discharge cycles, which is peculiar depending on the cell materials and microstructure. Such mechanical stress results in cracks and contact losses, especially in the case of ASBs with SIEs, which are not as elastic as SPEs and SLICs.

In a work by Koerver et al.,[39] the combination of several electrode active materials for ASBs was investigated from this angle. The pressure changes of the AMPs during galvanostatic cycling were monitored *in operando* (*Figure 7*). The cells were obtained by cold pressing, using LPS as the solid electrolyte and the binder for the CEs. LTO was used as the anode because of negligible strain upon lithiation/delithiation, so as to determine the neat volume change due to the cathode AMPs. As the volume changes correspond to changes in the SOC and in the lattice parameters of the AMPs, *in-situ* XRD at different SOC was used to extract the partial molar volume of lithium V_m (Li) upon cycling. In the case of layered materials, the V_m (Li) of a particular phase was treated a solution property and defined as the partial differential of the volume caused by adding lithium.
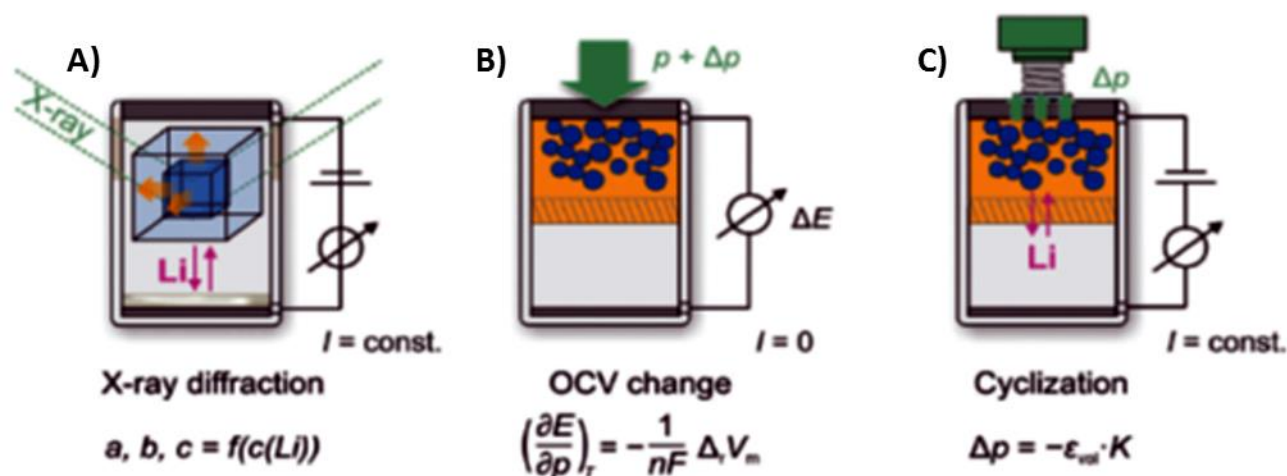
Figure 7. (A,B,C) Representation of the methods for the characterisation of the pressure induced stress at different SOC upon cycling: A) in-situ XRD, B) OCV monitoring, C) uniaxial in-situ measurement of the pressure. Reproduced, adapted and reprinted with permission from Ref 39.

The difference of V_m (Li) in both electrodes (upon discharge) was ultimately linked to the OCV based on thermodynamic considerations, and therefore correlated to the pressure and XRD data. A remarkable stress of ≈ 0.6 MPa was observed upon charge in LTO/LPS/LCO and LTO/LPS/NMC cells, with opposite signs due to LCO expansion and NMC contraction during delithiation. When LTO was replaced by a metal anode or graphite, the stress increased by one order of magnitude, which highlights the importance of proper material choice and the difficulty of suppressing delamination by the application of an external pressure.

3 CEs Fabrication methods

3.1 CEs with solid polymer electrolytes and single Li⁺ ion conductors

To ensure effective σ_i throughout cells with SPEs and SLICs, these latter are commonly used as the binder in the CE.[40] Common CEs with non-ionically conductive PVdF, sometimes with the addition of a lithium salt, are used as well. This is often the case also with CPE separators, so that the SIE particles are not included in the CE formulation. Differently from SIE-based cells, for which the preparation protocol is often detailed, the basic information about the process and mass loading with new CPEs is often lacking.[5]

3.1.1 Solvent casting. The most common binder in LIBs with LEs is PVdF, which displays excellent thermal and electrochemical stability. Anyway, PVdF is costly, poorly flexible and requires harmful solvents such as NMP for processing. Water-soluble alternatives have been experimented in recent years. In this regard, carboxyl methyl cellulose (CMC) (mostly its sodium salt) has been proven to be an effective binder for both cathodes and anodes.[41]

Solvent casting is commonly used to obtain SPE and SLIC films or electrode slurries containing them, and the process is almost analogous to that used for common PVdF-based CEs for LIBs. However, SPEs do not often display high thermal stability, therefore traces of solvent, unwelcome for a good stability at the interface with lithium metal anode, can be difficult to remove.[5] Moreover, the reactivity of the lithium salt with the current collector in the presence of the solvent and air moisture must be taken into account. There are also report of water-based slurries. By instance, SLICs consisting of copolymers with polyanionic blocks based on TFSI⁻ anion and EO units in the main chain[42] or as pendant[43] segments can be processed in water to obtain an ink-like slurry, which is casted on the current collector and dried under vacuum at relatively low temperature (50 °C).

3.1.2 Extrusion and dry blending. Extrusion is a consolidated and widespread process to obtain composites for a large variety of applications; therefore, it could represent an appealing method to obtain composite electrodes from the industrial point of view. The use of this process could be envisaged any time that a composite is obtained by mixing a paste-like melt, such as PEO-based polymer electrolyte. In this regard, Appetecchi et al.[26] developed and characterised PEO-based CEs by a dry, solvent-free procedure through hot-extrusion of powder mixtures followed by roll-mill calendering. The resulting cathode films were ≈ 100 – 180 μm thick. Prior processing, all the components of the electrolyte, namely PEO, $LiCF_3SO_3$ (EO/Li of 20), SP_c and $LiMn_2O_4$ (LMO) were dried and carefully sieved to break up or eliminate macro-aggregates into smaller powder granules. Finally, they were gently mixed in the desired proportions by ball milling for at least 12 h. The electrodes obtained with this method were thoroughly characterised by a variety of techniques (e.g., TGA, DMTA, density and porosity analyses) and their composition was optimised based on the transport properties obtained by EIS analysis. This is something not common in the field of ASBs with SPEs, despite it would be of great interest considering the significant outcome on the overall cell performance. The measurement of the CEs intrinsic viscosity helped in revealing a maximum eight fold reduction of PEO molecular

weight, resulting from the hot extrusion/cold calendering process, thereby implying chemical degradation upon processing.

Similarly to extrusion, dry blending does not imply the use of any solvent to be disposed at the end of the process and can be easily performed for lab-scale trials. By instance, this method has been experimented by Wetjen et al.[44] for blends of paste-like mixture of PEO, Pyr$_{14}$TFSI ionic liquid and LiTFSI with pre-mixed cathode AMPs and carbon black (*Figure 8*).[44] Active materials such as V$_2$O$_5$ and LFP have been tested to be used in combination with PEO-Pyr$_{14}$TFSI-based SPEs. The blend has been annealed at 100 °C, hot-pressed and cold-calendered, yielding a film 50 μm thick with average loading from 3 to 5 mg cm^{-2}. According to SEM analysis, this process allows electrolyte to fully embed and cover the AMPs.

3.1.3 *In-situ* polymerisation/reticulation. Direct *in-situ* reticulation or polymerisation of SPEs on the electrodes allows homogeneous surface coating, thus assuring an intimate contact at the SPE/AMP interface. This approach is particularly promising for electrodes consisting in active material particles submitted to pyrolysis in the presence of a binder or a conductive polymer so as to obtain an interconnected network of electron conductive carbon. By instance, this strategy (binder pyrolysis) has been used to buffer the volumetric changes of Si anode particles upon lithiation[45] or to obtain thin LFP electrode films.[46]

This technique has been proven particularly interesting for thin film batteries. By instance, UV-induced free-radical polymerisation of a methacrylic-based SPE directly formed over a sputtered V$_2$O$_5$ thin film cathode enabled long term (500 cycles) galvanostatic cycling and operation up to 10C rate of graphite/SPE/V$_2$O$_5$ and Li/SPE/V$_2$O$_5$.[47]

In-situ polymerisation can be also performed on Li metal anode. By instance, Chai et al.[48] coated a cellulose nonwoven placed onto the Li metal electrode with a solution of vinylene carbonate (VC), lithium bis(oxalate) borate (LiBOB) and azobisisobutyronitrile (AIBN) as the thermal radical initiator onto a cellulose nonwoven fabric. After in-situ polymerisation upon heating, the LCO CE was joined on top to assemble the cell.
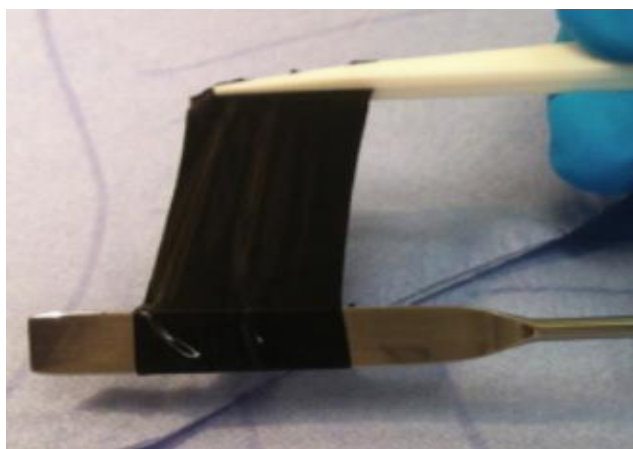

Figure 8. CE film obtained by dry blending and calendering a paste-like mixture of PEO, Pyr$_{14}$TFSI and LiTFSI with pre-mixed LFP powder and carbon black. Reproduced, adapted and reprinted with permission from Ref 44.

3.2 CEs with inorganic solid electrolytes (SIEs)

3.2.1 Hot pressing and sintering. The energy density of an ASB mainly depends on the thickness and configuration of the CE. In the case of all inorganic assembly, the latter is prepared beginning with the AMPs, SIE powder, and, depending on the σ$_e$ of the active material, an electron-conducting additive. The premixed powders are hot pressed to yield a pellet and sintered to reduce porosity and maximize the contact area between the SIE and the AMPs. The sintering temperature for oxide SIEs can reach 700-1000 °C in order to reduce the grain-boundary resistance. As previously mentioned, this method is challenging because of possible side reactions occurring at high temperatures.[49,50] Surface roughness affecting interfacial contact, high thickness (up to 1 mm), non-negligible porosity and resistive grain boundaries are the main problems connected with this method.[1,51] Grain boundaries are located at the interface between SIE grains with different crystal orientations arising from the sintering process and conditions.[50,52] Another problem of the powder pressing process is related to difficulties in large format production.[14] Moreover, oxide SIEs, including cubic garnet-type Li$_7$La$_3$Zr$_2$O$_{12}$ (LLZO, RT σ$_i$ ≈ 10^{-4} S cm^{-1}), require high sintering temperatures to allow intra-particle connection and densification, which can lead to degradation and side reactions, especially when the SIE powder is mixed with active material particles (AMPs) in CEs. On the other hand, sulfide SIEs can be sintered at RT, but processing them in inert atmosphere is currently impractical.[1,14]

3.2.2 Cold pressing. Differently from oxide SIEs, sulfide can be cold pressed to enable a good contact between the CE components. Anyway, hot pressing above the glass transition temperature of sulfide SIEs can be used to obtain dense pellets. A milling step aimed to reduce the particle size and increase the contact area is often performed. As mentioned before, surface coating on the active electrode material particles is often required to avoid high interfacial resistance and elemental cross-diffusion upon cycling.[49,50]

3.2.3 Wet coating. Wet chemical processing to obtain a composite cathode includes mixing, formation of a layer and compaction. A premixing of the AMPs, solid electrolyte precursor and conductive additive (if any) can improve mechanical contact, especially at low amounts of solid electrolyte and, thus, significantly increase cell performance (*Figure 9*A,B).[14,53]

The layer-forming step can be performed similarly to common LIB production, *viz.* casting the slurry on a current collector followed by solvent evaporation. In the case of sulfide SIEs, there are several issues specifically related to the sulphide chemistry, by instance because of the possible incompatibility with Cu current collectors and solvents such as NMP and water.[1] In order to enhance flexibility and mechanical stability, polymer binders might be added.[14] Anyway, the presence of insulating polymeric binders, such as nitrile-butadiene rubber (NBR), may partially block contacts between active materials and solid electrolytes (*Figure 9*C).[53] Volatile polymeric binders such as poly(propylene carbonate) (PPC),[54] which depolymerises by unzipping at low temperature (yielding a binder free CE after a heating step) have been experimented. At the same

time, there are reports of improved mechanical and electrochemical performance in the presence of binders such as ethyl cellulose,[55] implying that the effect of the polymeric phase is strictly dependent on the experimental conditions. Dissolution-precipitation technique in the absence of a polymeric binder has also been experimented. In this case, the AMPs and the conductive additive are dispersed in a solution of the solid electrolyte, which precipitates upon solvent evaporation to yield an homogeneous layer.[56]

Alternatively, a tape casting process can be used to cast the solution either onto a polymer tape or directly on the sintered SE separator, followed by a drying process in order to evaporate solvents.[14] In the former case, the polymer must be removed, thereafter. In the latter case, a screen-printing process and a preceding vacuum step is recommended to infiltrate the electrode slurry in the porous SE separator. Due to the shrinkage of the active material phase after solvent evaporation, the infiltration step has to be repeated several times.[14,15]

A third compaction step is required for electrode densification and to maximise contact among the components and the current collector. In this step, there is a trade-off between reducing porosity and avoid excessive stress, which could damage the AMPs. With sulfide SIE, this step can be performed by calendering, whereas, as already stated, oxide SIEs require high temperature sintering, causing possible side reaction and additional production costs.[14]

A high-viscosity process in the presence of a polymer binder can be also be used, yielding a flexible CE. In this case, the components are mixed at moderate temperatures and the CE layer is extruded through a slit. Co-extrusion can also be performed at industrial level, yielding joined composite electrode and solid electrolyte layers.[15] The high viscosity process could be compatible with the self-assembled block copolymer template method (*Figure 9*F) reported by Wakayama et al.[57] First the LCO and LLZO metal-organic precursors were dissolved with the copolymer. After the solvents evaporation, LCO and LLZO precursors were segregated into the different blocks of the copolymer. After the removal of the organic phase by annealing, nano-sized LCO was perfectly embedded in the LLZO matrix, yielding a highly dense and homogeneous CE (*Figure 9*D).[57]

3.2.4 Cold sintering. The cold sintering process has also been recently experimented for composite electrodes containing sulfide SIE (*Figure 9*E).[49] A liquid phase based on a volatile solvent able to finely dissolve the SIE is used to wet the component powder, which are then compacted under pressure. At the same time, the edges of the SIE particles are dissolved and re-precipitate into interstitial spaces, resulting in a dense pellet after complete solvent evaporation. The choice of the solvent is of paramount importance to avoid the formation of insulating, passivating phases.[49]
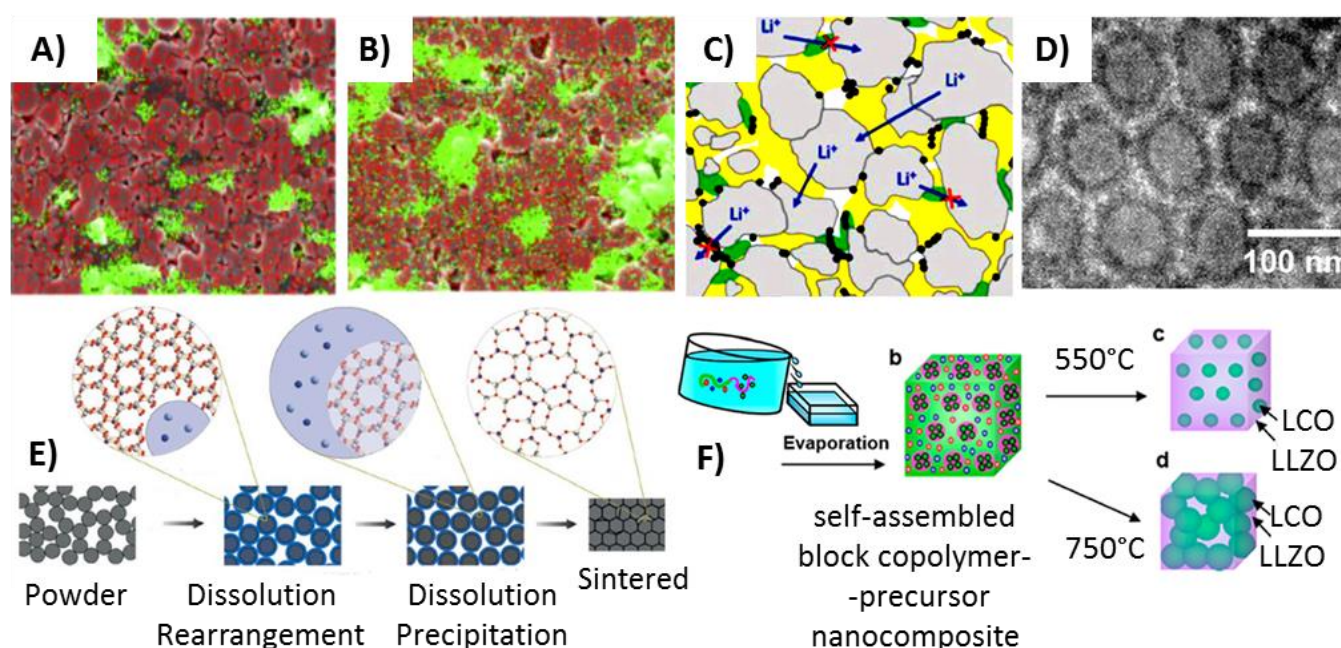

Figure 9 EDX elemental maps for Ni (red) and S (green) from cross-sections of CEs consisting of NMC, LPSC and NBR electrodes without (A) and with (B) premixing the powders. Reproduced, adapted and reprinted with permission from Ref 53. C) Schematic diagram representing the microstructure of a CE consisting of AMPs (grey), SIE (yellow), carbon NPs (black) and an insulating binder (green) blocking Li+ ion. Reproduced, adapted and reprinted with permission from Ref 53. D) FESEM analysis of the self-assembled nanocomposite block copolymer-precursors of LCO and LLZO. Reproduced, adapted and reprinted with permission from Ref 57. E) Schematic representation of the cold sintering dynamics. Reproduced, adapted and reprinted with permission from Ref 49. F) Preparation of the 3D nanocomposite consisting of LCO and LLZO from a self-assembled block copolymer template. Reproduced, adapted and reprinted with permission from Ref 57.

Journal Name

ARTICLE

3.2.5 Direct deposition methods. As mentioned before, AMP coating with protective layers is usually performed by wet processes. Anyway, direct deposition methods can be used, and coating with thin layers of SIE has also been experimented. By instance, sulfide SIE-coated LCO could operate in a graphite/SIE/LCO cell in absence of additional SIE in the CE, delivering a specific discharge capacity of 133 mAh g^{-1}. However, coating was performed by pulsed laser deposition (PLD), which is unlikely to be practical for large-scale production.[15]

Direct deposition methods have also been experimented for coating preformed SIE pellets with the AMPs. By instance, deposition of Si NPs on LLZO pellets has been attempted by sputtering.[58] A thin (≈ 45 nm) layer of Si deposited on LLZO (Ta-doped) has been found to display good adhesion (by *ex-situ* cross-sectional SEM analysis) and a capacity retention of 97 % after 100 galvanostatic cycles at C/10 (4 µA cm^{-2}) in a Li/LLZO/Si cell. Nevertheless, such a thin layer corresponds to an areal capacity of only 40 µAh cm^{-2}. With a 180 nm Si layer, the capacity retention has been found to be 85 % under the same condition (including the current density). With a 900 nm thick Si layer, cell failure has been observed in a few cycles, due to severe contact losses as confirmed by post-mortem cross-sectional SEM analysis.[58]

4 Interfacial compatibility

As discussed in the previous paragraph, many efforts have been dedicated to the development of preparation processes aimed to reduce porosity and improve the interfaces in CEs and ASBs. This is of paramount importance, especially when considering the requirements for scaling-up at the industrial level, and the main problems and envisaged solutions will be addressed in the next subsections.

4.1 Issues and challenges

Despite the excellent transport properties of many solid electrolytes, high internal resistance (at the grain-grain interface), capacity fading, poor rate capability and dendrite formation are often reported for lab-scale ASBs. The chemistry at the interface between the solid electrolyte and AMPs, together with the CE composition and morphology, play fundamental roles in these regards.[21] Poor contact at the AMPs/SIE interface results in reduced capacity and rate capability.[17] Besides the pores arising from the preparation process, the stress induced by volumetric expansion following consecutive charge and discharge cycles generates cracks at the AMPs/SIE interface. This affects the interfacial contact resistance ($R_{contact}$), which increases with decreasing the contact area ($A_{contact}$):

Equation 20) $$R_{contact} = \frac{L_{contact}}{\sigma_i \cdot A_{contact}}$$

where $L_{contact}$ is the interfacial thickness.[19]

The reduction of contact at the interface between the active material particles and the solid electrolyte upon cycling results in the electro-chemo-mechanical failure leading to capacity loss (*Figure 10C*).[59] In this regard, SPEs offer an advantage over SIEs, as the former allow good adhesion to AMPs and buffering the volumetric changes upon cycling. By instance, cathode LiFePO$_4$ (LFP) nanoparticles (NPs) encapsulated by a poly(ethylene glycol) (PEG)-based copolymer electrolyte demonstrated a remarkably improved cycling performance in Li/SPE/LFP lab scale cells, as compared to uncoated LFP NPs.[60] Also, low molecular weight (400-500 a. u.) PEG was incorporated as co-binder into composite V$_2$O$_5$ cathodes for LMPBs in order to improve the Li$^+$ transport properties through the electrode bulk.[61,62] However, the small PEG chains, unwelcome for the lithium anode, were proved diffusing through the polymer (PEO) electrolyte separator to reach and, therefore, degrading the Li metal surface. *Post mortem* analysis by scanning electron microscopy (SEM) of the cell revealed that despite the interface between the SPE separator and the CE was damaged in both cases, major cracks could be observed inside the CE with uncoated LFP NPs (*Figure 10*A,B).[60] It is worth mentioning here that the presence of void spaces is also detrimental at the interface with Li metal, to the point that dendrite formation has been observed in LLZO pellets upon galvanostatic Li deposition/dissolution in Li/LLZO/Li cells.[63,64] This, despite t_{Li+} in LLZO equals one and the shear modulus is one order of magnitude higher than the widespread reference value of 8.5 GPa from Monroe and Newman,[63,64] demonstrating that dendrite formation under this condition depends on microstructure.

Besides the issues arising from porosity, the resistance at the interface between the active material particles and solid electrolytes can also be affected by chemistry, in particular by the space-charge layer, element diffusion and side reactions.[65]

Space-charge layer related issues are peculiar to AMPs/SIEs interface, in particular with sulfide electrolytes and oxide cathode materials. In the latter case, the depletion of Li$^+$ ions occurs on the sulfide electrolyte side, leading to a high interfacial resistance.[1,17]

Element diffusion at the cathode AMP/SIE interface has been reported for both oxide and sulfide electrolytes. This phenomenon results in the formation of interlayers affecting Li$^+$ ion transport inside/outside of the AMPs. Electron conductive interlayers may also result as the products of side reactions. High pressure/temperature preparation processes and cell operation above the oxidation potential of the SIE have been proposed as possible causes for interfacial element diffusion and side reactions.[17] By instance, in the case of sulfide electrolytes, the formation of interlayers, detrimental to the cell performance, has been observed upon *post mortem* analysis after galvanostatic cycling (GC) with argyrodite-type Li$_6$PS$_5$Cl (LPSC, RT σ_i = 1.4 10^{-5} S cm^{-1}) and cathode LiCoO$_2$ (LCO) particles, or with Li$_2$S–P$_2$S$_5$ (LPS glass or glass/ceramic electrolyte with maximum

ARTICLE

σ_i for P_2S_5 content of 20-30%) and $LiNi_{0.8}Co_{0.15}Al_{0.05}O_2$ (NCA) cathode particles.[1] Element cross-diffusion and phase transition upon

processing the CE at high temperature has been reported at the interface between LLZO and LCO.
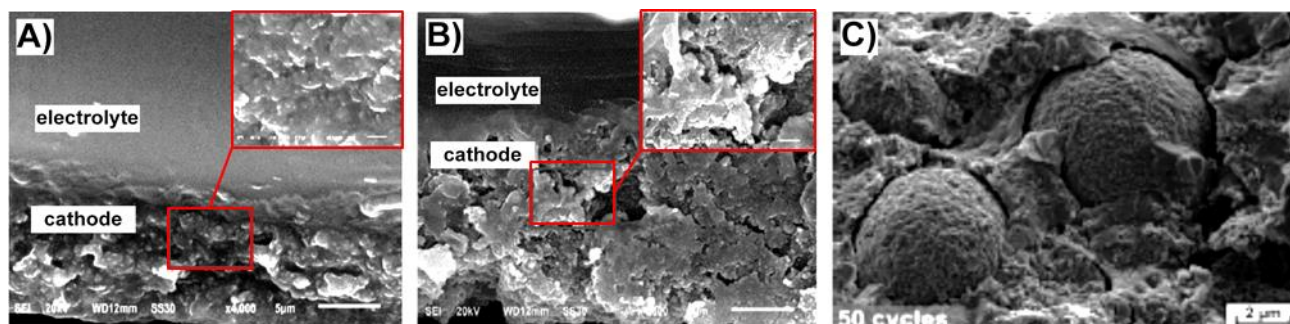

Figure 10. SEM analysis of the CE/SPE interface (cross-section) after 300 CG cycles at 1C with A) LFP NPs coated with a PEG-based copolymer B) uncoated LFP. Reproduced, adapted and reprinted with permission from Ref 60. SEM analysis of a CE consisting of NMC and Li3PS4 at SOC (State of Charge) = 0 after 50 CG cycles (C) displaying contact loss. Reproduced, adapted and reprinted with permission from Ref 59.

The phase transition consisted in the formation of less conductive (RT $\sigma_i \approx 10^{-6}$ S cm^{-1}) tetragonal LLZO.[66] Cubic Ta-doped LLZO has been found to react with commercial cathode AMPs upon annealing. According to X-ray diffraction (XRD) and Raman analysis, the degradation processes occur at 500 °C with LFP and $LiMn_2O_4$ (LMO), and at 700 °C with LCO and $LiNi_{0.33}Co_{0.33}Mn_{0.33}O_2$ (NMC).[67]

The oxidative degradation of SPEs and the polymer electrolyte fraction in CPEs results in the formation of side products. If these compounds do not form a good passivating layer, the continuous decomposition of the polymer matrix and/or the lithium salt occurring upon charge (delithiation) at high voltage leads to the increase of the cell resistance and poor capacity retention.[27] Solid electrolyte degradation due to electron conductive additives in CEs has also been reported. By instance, LGPS degradation at the interface with acetylene black (AB_c) has been found to occur above 4.5 V.[27]

4.2 Towards optimization and scaling-up

As mentioned in the previous paragraph, environmental sensitivity of several SIEs, especially sulfide electrolytes, is one of the major concern for industrial scale-up. In this regard, many efforts have been dedicated to address this issue by means of the use of additives during the synthesis, chemical substitution and surface coatings.[65] By instance, the evolution of H_2S gas from sulfide SIEs in humid environment has been suppressed upon the addition of FeS and CaO in LPS, or by substituting Sn with As in Li_4SnS_4.[15] Surface coating with LiF has been found to be effective in preventing the formation of insulating Li_2CO_3 on LLZO surface upon Li^+/H^+ exchange occurring upon exposure to air moisture.[68] Moreover, in the case of LLZO, chemical substitution and the incorporation of several different elements have been extensively used in order to improve σ_i and lower the grain boundary resistance.[69-71]

Surface coatings are also exploited to improve the chemical compatibility between solid electrolytes and AMPs and reduce the

interfacial resistance. Typical coatings are electron-insulating ion-conducting oxide materials. Anyway, electronically conductive coatings, such as NiS and CoS on LCO, have also been experimented. Ion conductive coatings, including oxide layers consisting in $Li_4Ti_5O_{12}$, $LiNbO_3$ and Al_2O_3, are commonly used to coat NMC and $LiCoO_2$ in order to avoid side reactions with sulfide SIEs and oxide such as LLZO.[1,15,50,72] A similar approach has been attempted to enable the use of polymer electrolytes above 4V. By instance, LATP has been used to coat LCO particles in lab-scale Li metal cells with a PEO-based SPE as the ion conductive binder and electrolyte separator.[73] The cycling performance at 60 °C was remarkably improved as compared to analogue cells devoid of LATP, with a capacity retention ≈ 93% (only 50 cycles are demonstrated, though).

In Li/LLZO (Ta doped)/NMC cells, Ketjen Black (KJ_c) and Super P (SP_c) carbon particles in the CE were found to promote the degradation of LiTFSI, resulting in the formation of Li_2CO_3. The cathode slurry contained NMC, the carbon particles, PVdF and LiTFSI. The latter was added to the cathode slurry to improve the ionic conductivity.[74,75] The use of vapour grown carbon fibres (VGCF), which results in lower reactivity towards LLZO, has been proposed as a possible solution.[74,75] Carbon additives have also been suggested to have a catalytic effect in the decomposition of PEO-based electrolytes. Thermogravimetric (TG) analysis of composite materials consisting of the electrolytes and different amount of SP_c revealed that the % weight loss depended on the carbon content.[26] A similar catalytic effect was found in ternary mixture of PEO, lithium bis(trifluoromethanesulfonyl)imide (LiTFSI) and the ionic liquid N-butyl-N-methylpyrrolidinium bis(trifluoromethane sulfonyl)imide (Pyr$_{14}$TFSI).[44]

SPE-based coatings have been experimented with silicon anodes. Si displays an outstanding theoretical specific capacity of 3579 mAh g^{-1} for $Li_{15}Si_4$ alloy, but the corresponding volume increment up to 300 % limits its practical application.[76] Capping amorphous Si NPs with PEG (24 EO units per chain) in CEs with SP_c and poly(vinylidene difluoride) (PVdF) as the binder was experimented to prevent

aggregation, buffer the volume changes and fasten Li$^+$ ion transfer (i.e., PEG was found to allow Li$^+$ diffusion) during the lithiation/delithiation cycles.[77] PVdF was chosen because of good compatibility with ethylene oxide-based SPEs. The Si anode was tested in lab scale Li/SPE/Si cells, where the SPE consisted of LiClO$_4$ in a mixture of PEO with PEO-PS copolymer. The best results were obtained with dimethyl phthalate (DMP) as plasticiser.[77] Synchrotron small-angle X-ray scattering (SAXS) and transmission electron microscopy (TEM) analysis of the electrode before and after cycling revealed that the homogeneous spacing between the NPs as well as their pristine characteristics were preserved, even though the NPs volume was increased by 300-400 %. Nevertheless, only 10 cycles were demonstrated, therefore the feasibility of such approach is far from being proved. Polymeric coatings and interlayers have also been experimented in order to improve the interfacial contact or compatibility of SPEs with the electrode materials. By instance, *in-situ* polymerisation of poly(ethylcyanoacrylate) (PECA) on LCO particles allowed increasing the delivered capacity and the cycling ability of lab-scale Li metal cells with a PEO-based electrolyte, as compared to uncoated LCO. Anyway a capacity fading of ≈ 50 % could be observed in ≈ 50 cycles at 80 °C.[74] Wider electrochemical stability window is offered by polymer matrixes other than pure PEO,[10] which is well known to oxidize around 3.8 V *vs.* the Li°/Li$^+$ redox couple.[78] By instance, poly(triethylene glycol carbonate) (PTEC) and poly(vinylene carbonate) (PVCA) have been shown to be compatible with 4V class LiFe$_{0.2}$Mn$_{0.8}$PO$_4$ (LFMP) and LCO.[48,79] Simonetti *et al*.[80] have exploited the ionic liquid phase separation, occurring in IL-rich (up to 60 % wt) PEO-based SPEs for promoting full (IL) coating onto the polymer host. Therefore, the so-obtained IL-coated PEO electrolyte was found to be able of operating with 4V cathodes (i.e., not directly in contact with PEO) without any polymer oxidation. Otherwise, dramatic capacity fading is observed in NCA and, especially, in NMC cathodes operating with PEO electrolytes.[44] In addition, the ionic liquid leakage, i.e., due to an IL fraction not coordinated by the lithium salt, enables the formation of 3D conductive networks through the SPE bulk, allowing conductivity values up to 3.5×10^{-4} S cm^{-1} already at –20 °C.

Besides Li$^+$ ion conducting matrixes, electron conductive polymers have also been proven effective (mostly with LEs) in buffering the volumetric expansion upon cycling or enhancing electron transport with poorly conductive active materials.[81] By instance, anode composites prepared by *in-situ* polymerisation of a polyaniline (PANI)-Si NPs hydrogel have allowed lab-scale cells achieving 5,000 cycles with over 90 % capacity retention at current density of 6.0 A g^{-1}.[82] Improved electronic conductivity (σ_e) following the *in-situ* polymerisation of polypyrrole (Ppy) or PANI on poorly conductive LFP particles has also been reported.[83] As an additional example, the σ_e of cold sintered (see above) V$_2$O$_5$, could be successfully improved by two orders of magnitude by adding 1–2 vol % of poly(3,4-ethylenedioxythiophene) polystyrene sulfonate (PEDOT:PSS) during sintering at 120 °C.[49,55]

Mixed-conductive polymers have also been demonstrated to work in lab-scale cells. The block copolymer poly(3-hexylthiophene)-poly(ethylene oxide) (P3HT-PEO) with LiTFSI displays appreciable

both electronic (σ_e) and Li$^+$ conductivity. By instance, the σ_e was found to vary from 10^{-7} to 10^{-3} S cm^{-1} depending on the P3HT oxidation level, that is the molar ratio between the electrons extracted from the polymer and the 3HT moieties. Being the σ_e at a minimum value at low oxidation level, an additional advantage of this material as a binder would be overdischarge protection.[84] LiTFSI doped P3HT-PEO was used as the binder in a Li/SPE/LFP. The SPE consisted of LiTFSI doped polystyrene-b-poly(ethylene oxide)-b-polystyrene copolymer (SEOS). As a proof of concept, the cell could deliver a discharge capacity of 170 mAhg^{-1} (i.e. full capacity) at upon galvanostatic cycling at 0.02 mAcm^{-2}, but only four cycles were demonstrated.[85]

A subsequent combination of experimental an simulation studies evidenced that the transport properties of the block copolymer are not suitable for application, being with a maximum discharge capacity of 5 mAhg^{-1} at C/5 rate.[20]

Layered cell architecture have also been experimented. By instance, a SPE consisting in LiTFSI salt and cross-linked poly(ethylene glycol) methyl ether acrylate (CPMEA) has been used as interlayer on both sides of LATP pellets to yield a sandwiched hybrid electrolyte (PCPSE). This strategy enabled the use of LATP with Li metal and allowed achieving improved cycling performance at 65 °C. Lab-scale Li/PCPSE/LFP and Li/CPMEA/LFP cells (only the CPMEA electrolyte was used as the binder in the CE) displayed capacity retention values of ≈ 77 and 54 % after 640 and 325 galvanostatic cycles, respectively.[86] Layered cell architectures have also been experimented joining different SPEs. By instance, the superior electrochemical stability of poly(N-methyl-malonic amide) (PMA) and the good compatibility of PEO-LiTFSI SPE with Li metal have been simultaneously exploited in the cell configuration Li/PEO-LiTFSI/PMA/LCO. Both the SPE layers contained LiTFSI and Poly(vinylidene fluoride-co-hexafluoropropylene) (PVdF-HFP) to improve the film-forming ability. A mixture of PVdF, PMA and LiTFSI was used as binder in the composite cathode.[87]

5 Considerations and future trends

The actual market including large-scale applications such automotive and electrochemical storage from renewable sources, requires Li-based devices with larger gravimetrical energy, thus addressing the search for electrolyte systems able to operate at voltage higher with respect to that of the conventional alkyl carbonate solutions,[88] with sufficient operational life and safety. The targets written in the EU initiatives as the Strategic Energy Technology Plan (SET Plan for 'Batteries'), aims at energy densities >350 Wh kg^{-1} and >1000 Wh L^{-1} for the next-generation of Li-ion secondary batteries, and even higher >400 Wh kg^{-1} and >1200 Wh L^{-1} are aimed for the next-generation of secondary batteries comprising a Li-metal anode, with fast charge rates above 10C and power density values >10000 W kg^{-1} as 2030 target.

Regarding materials and components for Li$^+$-ion conducting electrolytes, a few main trends are worth to be mentioned, particularly a gained stability towards oxidation (anodic) which would allow the use of higher (from 4 to 5 V) voltage cathodes, i.e.,

$LiNi_xMn_{2-x}O_2$ spinel or LiMPO4 (M = Ni, Co, Mn), capable of granting larger cell specific energy and power values. For instance, a wide electrochemical stability window is aimed for both strong oxidizing cathodes and remarkably reducing anodes. In this scenario, F-containing organic compounds (generally, ethers and alkyl carbonates)[89] and lithium salts,[90,91] seem rather promising because of the remarkable electron-withdrawing effect of the fluorine atom. In addition, these F-based compounds exhibit good film-forming ability onto carbonaceous, silicon and lithium anodes.

A deeper and deeper knowledge of the electrolyte composition within the electrode pores is needed to design properly optimized formulations. Recently, Kiyohara et al.[92] reported the results of Monte Carlo simulations for electrolytes loaded into porous electrodes, showing strong dependence of their electrical peculiarities on the pore size and the dielectric constant. For instance, going from low to high dielectric constant value, the porous electrode capacitance is found to be fully reversible. With decreasing the pore size, a capacitance increase is expected for low dielectric constant electrolytes whereas, for high dielectric constant values, the capacitance is expected to decrease. The dependence on the pore size can be explained in terms of balance among the electrostatic interactions and those due to the volume exclusion within the porous electrode. However, the behaviour might substantially differ for non-liquid electrolytes i.e., gels, polymeric and solid-state, as well as for those composed of solely ions, i.e., ionic liquid electrolytes.

Ceramic electrolytes are very appealing candidates for producing all-solid-state, highly safe batteries particularly considering that a few of them exhibit room temperature ionic conductivity exceeding 10^{-3} S cm^{-1}.[93] However, the performance of these electrolyte systems is still limited by remarkable resistance at the grain-grain interface, i.e., depleting the overall ion conduction, fragility issue when up-scaled and modest interfacial contact with electrodes. Hybrid electrolytes, obtained by suitably combining ceramic ion conductors with ionic liquids or polymeric systems, have been proposed for overcoming the shortage of the solid electrolytes. However, recent published papers have demonstrated how simply blending ceramic electrolytes with ionic liquids[94] or polymers[95] does not result into any synergic effect on the ion transport properties, evidencing the existence of an energy barrier at the ceramic/ionic liquid (or polymer) interface, which could be waived by proper functionalization of the materials.

The need of deep understanding the behaviour at the electrolyte/electrode interface, in conjunction with a thorough surface characterization, has increases in the last years the interest on and application of simulations and calculations to the research on the Li-ion technologies. For instance, the knowledge regarding the fundamental chemistry of the Li-ion batteries, especially applied to the electrolytes and the solid electrolyte interphase, may strongly gain benefits from the application of atomistic level methods. Ferguson and Curtiss[96] have presented an extensive approach in a review focused on atomic-level computations and simulations, on the chemistry of the Li$^+$ electrolyte organic solvents, combined with: i) the application of quantum chemical methods for investigating the

reactions of organic solvents and designing an oligomer SEI layer model and ii) data from ab initio calculations for screening electrolytes to be addressed to high operating potential values.

In the push for better batteries constantly driven by many industries, one of the primary drivers behind the massive market intrusion of solid state batteries is to enable the use of lithium metal as the anode, which can provide almost ten times the gravimetric capacity (Ah g^{-1}) of the currently used carbon anode, with a neat improvement in the overall energy density of the final device. In this respect, non-flammable, highly conducting electrolyte materials and components capable of allowing the efficient and safe use of lithium metal anodes are fundamental as well as the formation (and maintaining upon cycling) of an intimate contact at the solid-solid interface and, concurrently, mitigate the surface reactivity of the various components. Among the approaches to address the solid-solid contact issue include, we envisage the fabrication of high-pressure cells in robust packaging to maintain the contact even upon volume changes occurring during cycling, the preparation of easy processable SEs (e.g., by solvent-free extrusion or solution processing) to optimally wet the electrode active material surface and enhancing the conductive pathways,[97] and even adding a gel or liquid to form a hybrid interfacial film that can accomodate the dynamic gap between the two solid surfaces during operation.[98] Room temperature ionic liquids (RTILs) may surely help in this respect. A few papers[99-103] have reported beneficial effects of IL-based electrolytes in mitigating/minimizing the undesired behaviours, such as polysulfide dissolution and precipitation onto to the lithium anode, self-discharge, occurring in lithium-sulphur devices, besides improving the battery safety issue. IL-containing polymer electrolyte systems are expected to behave even better, especially in minimizing the polysulfide shuttle mechanism. Properly designed ionic liquid/organic formulations[103] could allow better electrochemical performance with respect to pure RTILs, especially in terms of ion transport properties and high rate battery cycling, without depleting the fundamental safety requirement.

6 Conclusions

Solid electrolytes are promising materials with excellent transport properties, which could allow battery operation in a wide operating temperature range, provide longer cycle life, improved safety and higher energy density as compared to commonly available Li-ion batteries.

The complex interfacial chemistry and processes in ASBs as discussed herein have to be improved in order to achieve high enough energy density to outperform LE based systems. The selection of compatible materials is particularly critical for both the electrochemical performance and the cycle life, due to the interfacial chemistry and the combined impact on the electro-chemo-mechanical stress over cycling. Composite and layered systems are promising from this point of view because they allow meeting different requirements and tuning the characteristics of the components depending on the interface at play.

Once the chemistry of a cell has been selected, including materials, composition and structure, a fundamental question, as detailed in

this work, on how to develop the wide-scale adaptation (upscaling and packaging) still waits for an answer from the scientific community.

Materials chemistry considerations go hand in hand with the architecture and arrangement of the composite electrodes and electrolytes. As we discussed, the microstructural characteristics have a profound impact on the transport properties and, ultimately, on the cell performance. Several factors, including the morphology of the starting materials, and the preparation process affect the microstructure. As a result, to better understand the combined effect of these parameters on the cell performance, a multivariate approach, possibly complemented to *in-situ* and *in-operando* techniques, is likely to be very much effective.

To enable the large-scale market production of truly solid-state batteries, which is crucial to provide effective solutions to the global need of extremely high-performing electrochemical energy storage systems, a seamless integration of the battery components can be envisaged through the assembly of an ordered architecture layer-by-layer on shaped surfaces easily adaptable to many device shapes. Advancements in the fabrication processes is thus fundamental for Li-based technology to remain the main solution for electric power systems to definitely jump into the modern green technology revolution.

List of Abbreviations and Acronyms

AB_c = acetylene black

$A_{contact}$ = contact area

AIBN = azobisisobutyronitrile

AMPs = active material particles

ASBs = all solid batteries

C_{dl} = double layer capacitance

CB = carbon black

CEs = composite electrodes

CMC = carboxyl methyl cellulose

CPEs = composite polymer electrolytes

CPMEA = cross-linked poly(ethylene glycol) methyl ether acrylate

DC = direct current

D_{Li+} = diffusion coefficient of Li^+ in the electrolyte

$D_{Li+,composite}$ = diffusion coefficient of Li^+ in the composite

DMP = dimethyl phthalate

EDX = energy-dispersive X-ray

EIS = electrochemical impedance spectroscopy

EtC = ethyl cellulose

EVs = electric vehicles

FIB-SEM = focused ion-beam scanning electron microscopy

GC = galvanostatic cycling

KJ_c = Ketjen Black

LATP = $Li_{1+x}Al_xTi_{2-x}(PO_4)_3$

LCO = $LiCoO_2$

LEs = liquid electrolytes

LFMP = $LiFe_{0.2}Mn_{0.8}PO_4$

LFP = $LiFePO_4$

LGPS = $Li_{10}GeP_2S_{12}$

LiBOB = lithium bis(oxalate) borate

LIBs = Lithium ion batteries

LIM = 1 g UIO67 in 1.5 mL of LiTFSI in EMImTFSI

LIM-LLZO = mix of LIM (20%) and LLZO (80%)

LiTFSI = Lithium bis(trifluoromethanesulfonyl)imide

LLTO = $Li_{3x}La_{2/3-x}TiO_3$

LLZO = cubic garnet-type oxide SIE $Li_7La_3Zr_2O_{12}$

LMO = $LiMn_2O_4$

LMPB = lithium metal polymer batteries

LPS = $Li_2S–P_2S_5$

LPSC = Li_6PS_5Cl

LSPSC = $Li_{9.54}Si_{1.74}P_{1.44}S_{11.7}Cl_{0.3}$

LTO = $Li_4Ti_5O_{12}$

NBR = nitrile-butadiene rubber

NCA = $LiNi_{0.8}Co_{0.15}Al_{0.05}O_2$

NMC = $LiNi_{0.33}Co_{0.33}Mn_{0.33}O_2$

NMP = N-methyl pyrrolidone

NPs = nanoparticles

P3HT-PEO = Poly(3-hexylthiophene)-Poly(ethylene oxide)

PANI = polyaniline

PCPSE = sandwiched hybrid electrolyte

PECA = poly(ethylcyanoacrylate)

PEDOT:PSS = poly(3,4-ethylenedioxythiophene) polystyrene sulfonate

PEG = poly(ethylene glycol)

PEO = poly(ethylene oxide)

PLD = pulsed laser deposition

PMA = Poly(N-methyl-malonic amide)

PPC = poly(propylene carbonate)

Ppy = polypyrrole

PTEC = poly(triethylene glycol carbonate)

PVCA = poly(vinylene carbonate)

PVdF = poly(vinylidene difluoride)

PVdF-HFP = Poly(vinylidene fluoride-co-hexafluoropropylene)

$Pyr_{14}TFSI$ = 1-butyl-4-methyl pyrrolidinium bis(trifluoromethanesulfonyl)imide

q = capacity density of the CE

$R_{contact}$ = interfacial contact resistance

R_e = resistance to electron diffusion

r_{ion} = resistance to ion diffusion

R_{Li+} = resistance to Li^+ ion transport

RT = room temperature

SAXS = Synchrotron small-angle X-ray scattering

SE = solid electrolyte

SEM = scanning electron microscopy

SEOS = polystyrene-b-poly(ethylene oxide)-b-polystyrene copolymer

SIEs = Solid inorganic electrolytes

SLICs = single Li+ ion conductors

SP_c = Super P carbon particles

SPEs = solid polymer electrolytes

speXL = photo-crosslinked PEO-LiTFSI-PYR_{14}TFSI

SS = stainless steel

Journal Name ARTICLE

t_d = time at which the cell reaches V_{cutoff}

TEM = transmission electron microscopy

TG = Thermogravimetric

t^{Li+} = Li^+ transference number

TLM = transmission line model

U^θ = open circuit potential of the active material

UIO-67 = (MOF based on Zr and 4,4-biphenyldicarboxylicacid)

VC = vinylene carbonate

V_{cutoff} = cut-off voltage

VGCF = vapour grown carbon fibers

$V_m(Li)$ = partial molar volume of lithium

XRD = X-ray diffraction

ε = electrolyte volume fraction

σ_e = electronic conductivity

σ_i = ionic conductivity

$\sigma_{i,composite}$ = ionic conductivity of the composite

τ = tortuosity

Conflicts of interest

There are no conflicts to declare.

Acknowledgements

References

1   K. H. Park, Q. Bai, D. H. Kim, D. Y. Oh, Y. Zhu, Y. Mo and Y. S. Jung, *Advanced Energy Materials*, 2018, **8**, 1800035.
2   Y.-S. Hu, *Nature Energy*, 2016, **1**, 16042.
3   J. Cabana, B. J. Kwon and L. Hu, *Accounts of chemical research*, 2018, **51**, 299–308.
4   M. J. Loveridge, G. Remy, N. Kourra, R. Genieser, A. Barai, M. J. Lain, Y. Guo, M. Amor-Segan, M. A. Williams, T. Amietszajew and others, *Batteries*, 2018, **4**, 3.
5   M. Keller, A. Varzi and S. Passerini, *Journal of Power Sources*, 2018, **392**, 206–225.
6   Z. Gadjourova, Y. G. Andreev, D. P. Tunstall and P. G. Bruce, *Nature*, 2001, **412**, 520–523
7   D. Brandell, PhD Thesis, Uppsala University, Department of Materials Chemistry, 2005.
8   P.-J. Alarco, Y. Abu-Lebdeh, A. Abouimrane and M. Armand, *Nature Materials*, 2004, **3**, 476–481..
9   L.-Z. Fan, Y.-S. Hu, A. J. Bhattacharyya and J. Maier, *Advanced Functional Materials*, 2007, **17**, 2800–2807
10 J. Mindemark, M. J. Lacey, T. Bowden and D. Brandell, *Progress in Polymer Science*, 2018, **81**, 114–143.
11 J. C. Bachman, S. Muy, A. Grimaud, H.-H. Chang, N. Pour, S. F. Lux, O. Paschos, F. Maglia, S. Lupart, P. Lamp, et al., *Chemical Reviews*, 2016, **116**, 140–162.
12 Y. Kato, S. Hori, T. Saito, K. Suzuki, M. Hirayama, A. Mitsui, M. Yonemura, H. Iba and R. Kanno, *Nature Energy*, 2016, **1**, 16030.

13 C. Cao, Z.-B. Li, X.-L. Wang, X.-B. Zhao and W.-Q. Han, Frontiers in Energy Research, 2014, 2, 25.
14 J. Schnell, T. Günther, T. Knoche, C. Vieider, L. Köhler, A. Just, M. Keller, S. Passerini and G. Reinhart, *Journal of Power Sources*, 2018, **382**, 160–175.
15 Y. S. Jung, D. Y. Oh, Y. J. Nam and K. H. Park, *Israel Journal of Chemistry*, 2015, **55**, 472–485.
16 C. K. Chan, T. Yang and J. M. Weller, *Electrochimica Acta*, 2017, **253**, 268–280.
17 J. Wan, J. Xie, D. G. Mackanic, W. Burke, Z. Bao and Y. Cui, *Materials Today Nano*.
18 D. T. Hallinan, I. Villaluenga and N. P. Balsara, MRS Bulletin, 2018, 43, 759–767.
19 L. Bai, W. Xue, Y. Li, X. Liu, Y. Li and J. Sun, *Ceramics International*, 2018, **44**, 7319–7328.
20 S.-L. Wu, A. E. Javier, D. Devaux, N. P. Balsara and V. Srinivasan, *Journal of The Electrochemical Society*, 2014, **161**, A1836–A1843.
21 K. Kerman, A. Luntz, V. Viswanathan, Y.-M. Chiang and Z. Chen, *Journal of The Electrochemical Society*, 2017, **164**, A1731–A1744.
22 N. Wolff, F. Röder and U. Krewer, *Electrochimica Acta*, 2018, **284**, 639–646.
23 F. L. Usseglio-Viretta, A. Colclasure, A. N. Mistry, K. P. Y. Claver, F. Pouraghajan, D. P. Finegan, T. M. Heenan, D. Abraham, P. P. Mukherjee, D. Wheeler and others, *Journal of The Electrochemical Society*, 2018, **165**, A3403–A3426.
24 W. Zhang, D. A. Weber, H. Weigand, T. Arlt, I. Manke, D. Schröder, R. Koerver, T. Leichtweiss, P. Hartmann, W. G. Zeier and others, *ACS applied materials & interfaces*, 2017, **9**, 17835–17845.
25 F. Strauss, T. Bartsch, L. de Biasi, A.-Y. Kim, J. Janek, P. Hartmann and T. Brezesinski, *ACS Energy Letters*, 2018, **3**, 992–996.
26 G. Appetecchi, M. Carewska, F. Alessandrini, P. Prosini and S. Passerini, *Journal of The Electrochemical Society*, 2000, **147**, 451–459.
27 J. Ma, B. Chen, L. Wang and G. Cui, *Journal of Power Sources*, 2018, **392**, 94–115.
28 J. Maier, *Progress in Solid State Chemistry*, 1995, **23**, 171–263.
29 L. Zhang, X. Zhan, Y.-T. Cheng and M. Shirpour, *The Journal of Physical Chemistry Letters*, 2017, **8**, 5385–5389.
30 T. Asano, S. Yubuchi, A. Sakuda, A. Hayashi and M. Tatsumisago, *Journal of The Electrochemical Society*, 2017, **164**, A3960–A3963.
31 D. Hlushkou, A. E. Reising, N. Kaiser, S. Spannenberger, S. Schlabach, Y. Kato, B. Roling and U. Tallarek, *Journal of Power Sources*, 2018, **396**, 363–370.
32 N. Kaiser, S. Spannenberger, M. Schmitt, M. Cronau, Y. Kato and B. Roling, *Journal of Power Sources*, 2018, **396**, 175–181.
33 Z. Siroma, T. Sato, T. Takeuchi, R. Nagai, A. Ota and T. Ioroi, *Journal of Power Sources*, 2016, **316**, 215–223.
34 M. Ménétrier, I. Saadoune, S. Levasseur and C. Delmas, *Journal of Materials Chemistry*, 1999, **9**, 1135–1140.
35 Y. Kato, S. Shiotani, K. Morita, K. Suzuki, M. Hirayama and R. Kanno, *The journal of physical chemistry letters*, 2018, **9**, 607–613.
36 B. Tjaden, S. J. Cooper, D. J. Brett, D. Kramer and P. R. Shearing, *Current Opinion in Chemical Engineering*, 2016, 12, 44–51.
37 P. Braun, C. Uhlmann, M. Weiss, A. Weber and E. Ivers-Tiffée, Journal of Power Sources, 2018, 393, 119–127.
38 M. Finsterbusch, T. Danner, C.-L. Tsai, S. Uhlenbruck, A. Latz and O. Guillon, *ACS Appl. Mater. Interfaces*, 2018, 10, 22329–22339.
39 R. Koerver, W. Zhang, L. de Biasi, S. Schweidler, A. Kondrakov, S. Kolling, T. Brezesinski, P. Hartmann, W. Zeier and J. Janek, *Energy & Environmental Science*, 2018, **11**, 2142–2158.

40 H. Zhang, C. Li, M. Piszcz, E. Coya, T. Rojo, L. M. Rodriguez-Martinez, M. Armand and Z. Zhou, *Chemical Society Reviews*, 2017, **46**, 797–815.

41 S. Srivastava, J. L. Schaefer, Z. Yang, Z. Tu and L. A. Archer, *Adv. Mater.*, 2013, **26**, 201–234.

42 R. Bouchet, S. Maria, R. Meziane, A. Aboulaich, L. Lienafa, J.-P. Bonnet, T. N. Phan, D. Bertin, D. Gigmes, D. Devaux and others, *Nature materials*, 2013, **12**, 452.

43 L. Porcarelli, A. S. Shaplov, M. Salsamendi, J. R. Nair, Y. S. Vygodskii, D. Mecerreyes and C. Gerbaldi, *ACS applied materials & interfaces*, 2016, **8**, 10350–10359.

44 M. Wetjen, G.-T. Kim, M. Joost, G. B. Appetecchi, M. Winter and S. Passerini, *Journal of Power Sources*, 2014, **246**, 846–857.

45 D. M. Piper, J. H. Woo, S.-B. Son, S. C. Kim, K. H. Oh and S.-H. Lee, *Advanced Materials*, 2014, **26**, 3520–3525.

46 N. Zhou, Y. Liu, J. Li, E. Uchaker, S. Liu, K. Huang and G. Cao, *Journal of Power Sources*, 2012, **213**, 100–105.

47 C. Gerbaldi, M. Destro, J. R. Nair, S. Ferrari, I. Quinzeni and E. Quartarone, *Nano Energy*, 2013, **2**, 1279–1286.

48 J. Chai, Z. Liu, J. Ma, J. Wang, X. Liu, H. Liu, J. Zhang, G. Cui and L. Chen, *Advanced Science*, 2017, **4**, 1600377.

49 Y. Liu, Q. Sun, D. Wang, K. Adair, J. Liang and X. Sun, *Journal of Power Sources*, 2018, **393**, 193–203.

50 Z. Gao, H. Sun, L. Fu, F. Ye, Y. Zhang, W. Luo and Y. Huang, *Advanced Materials*, 2018, **30**, 1705702.

51 Y. Ren, K. Chen, R. Chen, T. Liu, Y. Zhang and C.-W. Nan, *Journal of the American Ceramic Society*, 2015, **98**, 3603–3623.

52 Y. Kim, H. Jo, J. L. Allen, H. Choe, J. Wolfenstine and J. Sakamoto, *Journal of the American Ceramic Society*, 2016, **99**, 1367–1374.

53 Y. J. Nam, D. Y. Oh, S. H. Jung and Y. S. Jung, *Journal of Power Sources*, 2018, **375**, 93–101.

54 M. Yamamoto, Y. Terauchi, A. Sakuda and M. Takahashi, *Scientific Reports*, 2018, **8**, 1212.

55 J. Zhang, H. Zhong, C. Zheng, Y. Xia, C. Liang, H. Huang, Y. Gan, X. Tao and W. Zhang, *Journal of Power Sources*, 2018, **391**, 73–79.

56 N. C. Rosero-Navarro, A. Miura and K. Tadanaga, *Journal of Power Sources*, 2018, **396**, 33–40.

57 H. Wakayama, H. Yonekura and Y. Kawai, *Chem. Mater.*, 2016, **28**, 4453–4459.

58 C. Chen, Q. Li, Y. Li, Z. Cui, X. Guo and H. Li, *ACS applied materials & interfaces*, 2018, **10**, 2185–2190.

59 R. Koerver, I. Aygün, T. Leichtwei\s s, C. Dietrich, W. Zhang, J. O. Binder, P. Hartmann, W. G. Zeier and J. Janek, *Chemistry of Materials*, 2017, **29**, 5574–5582.

60 H. Zeng, X. Ji, F. Tsai, Q. Zhang, T. Jiang, R. K. Li, H. Shi, S. Luan and D. Shi, *Solid State Ionics*, 2018, **320**, 92–99.

61 P. Villano, M. Carewska, G.B. Appetecchi and S. Passerini, *Journal of The Electrochemical Society*, 2001, **149**, A1282-A1285.

62 G.B. Appetecchi, J.-H. Shin, F. Alessandrini and S. Passerini, *Journal of Power Sources*, 2005, **143**, 236-242.

63 Y. Ren, Y. Shen, Y. Lin and C.-W. Nan, *Electrochemistry Communications*, 2015, **57**, 27–30.

64 F. Shen, M. B. Dixit, X. Xiao and K. B. Hatzell, *ACS Energy Letters*, 2018, **3**, 1056–1061.

65 K. Nie, Y. Hong, J. Qiu, Q. Li, X. Yu, H. Li and L. Chen, Frontiers in Chemistry, 2018, **6**, 616.

66 K. Park, B.-C. Yu, J.-W. Jung, Y. Li, W. Zhou, H. Gao, S. Son and J. B. Goodenough, *Chemistry of Materials*, 2016, **28**, 8051–8059.

67 Y. Ren, T. Liu, Y. Shen, Y. Lin and C.-W. Nan, *Journal of Materiomics*, 2016, **2**, 256–264.

68 Y. Li, B. Xu, H. Xu, H. Duan, X. Lü, S. Xin, W. Zhou, L. Xue, G. Fu, A. Manthiram and others, *Angewandte Chemie International Edition*, 2017, **56**, 753–756.

69 V. Thangadurai, S. Narayanan and D. Pinzaru, *Chemical Society Reviews*, 2014, **43**, 4714.

70 S. Kumazaki, Y. Iriyama, K.-H. Kim, R. Murugan, K. Tanabe, K. Yamamoto, T. Hirayama and Z. Ogumi, *Electrochemistry communications*, 2011, **13**, 509–512.

71 R. Chen, W. Qu, X. Guo, L. Li and F. Wu, *Materials Horizons*, 2016, **3**, 487–516.

72 J. W. Fergus, *Journal of Power Sources*, 2010, **195**, 4554–4569.

73 Q. Yang, J. Huang, Y. Li, Y. Wang, J. Qiu, J. Zhang, H. Yu, X. Yu, H. Li and L. Chen, *Journal of Power Sources*, 2018, **388**, 65–70.

74 J. Ma, Z. Liu, B. Chen, L. Wang, L. Yue, H. Liu, J. Zhang, Z. Liu and G. Cui, *Journal of The Electrochemical Society*, 2017, **164**, A3454–A3461

75 F.M. Du, N. Zhao, R. Fang, Z.H. Cui, Y.-Q. Li, *Journal of Inorganic Materials*, 2018, **33**, 462.

76 Ozanam and M. Rosso, *Materials Science and Engineering: B*, 2016, **213**, 2–11.

77 I. Choi, H. Ahn and M. J. Park, *Macromolecules*, 2011, **44**, 7327–7334.

78 P.P. Prosini, S. Passerini, R. Vellone and W.H. Smyrl, *Journal of Power Sources*, 1998, **75**, 73-83.F.

79 W. He, Z. Cui, X. Liu, Y. Cui, J. Chai, X. Zhou, Z. Liu and G. Cui, *Electrochimica Acta*, 2017, **225**, 151–159.

80 E. Simonetti, M. Carewska, M. Di Carli, M. Moreno, M. De Francesco and G.B. Appetecchi, *Electrochimica Acta*, 2017, **235**, 323-331.

81 S. Ferrari, J. Nair, Y. Zhou and C. Wan, in *Polymer-based Nanocomposites for Energy and Environmental Applications*, Elsevier, 2018, pp. 283–313.

82 H. Wu, G. Yu, L. Pan, N. Liu, M. T. McDowell, Z. Bao and Y. Cui, *Nature communications*, 2013, **4**, 1943.

83 Y.-H. Huang and J. B. Goodenough, *Chemistry of Materials*, 2008, **20**, 7237–7241.

84 S. N. Patel, A. E. Javier and N. P. Balsara, *ACS Nano*, 2013, **7**, 6056–6068.

85 A. E. Javier, S. N. Patel, D. T. Hallinan, V. Srinivasan and N. P. Balsara, *Angewandte Chemie International Edition*, 2011, **50**, 9848–9851.

86 W. Zhou, S. Wang, Y. Li, S. Xin, A. Manthiram and J. B. Goodenough, *Journal of the American Chemical Society*, 2016, **138**, 9385–9388.

87 W. Zhou, Z. Wang, Y. Pu, Y. Li, S. Xin, X. Li, J. Chen and J. B. Goodenough, *Advanced Materials*, 2018, 1805574.

88 Q. Li, J. Chen, L. Fan, X. Kong and Y. Lu, *Green Energy & Environment,* 2016, **1**, 18-42.

89 Z. Zhang, L. Hu, H. Wu, W. Weng, M. Koch, P.C. Redfern, L.A. Curtiss and K. Amine, *Energy & Environment Science*, 2013, **6**, 1806-1810.

90 Z. Chen, Y. Ren, A.N. Jansen, C.K. Lin and W. Weng, K. Amine, *Nature Communications*, 2013, **4**, 66-78.

91 A. von Cresce and K. Xu, *Journal of Electrochemical Society*, 2011, **158**, A337-A342.

92 K. Kiyohara, T. Sugino and K. Asaka, *Journal of Chemical Physics*, 2010, **132**, 144705-144717.

93 J. Awaka, N. Kijima, H. Hayakawa and J. Akimoto, *Journal of Solid State Chemistry*, 2009, **182**, 2046-2052.

94 C. de la Torre Gamarra, G.B. Appetecchi, U. Ulissi, A. Varzi, A. Varez Alvarez and S. Passerini, *Journal of Power Sources*, 2018, **383**, 157-163.

95 M. Keller, G.B. Appetecchi, G.-T. Kim, V. Sharova, M. Schneider, J. Schuhmacher, A. Roters and S. Passerini, *Journal of Power Sources*, 2017, **353**, 287-297.

96 G. Ferguson and L.A. Curtiss, *Applications of Molecular Modeling to Challenges in Clean Energy*, American Chemical Society, distributed in print by Oxford Univerisity Press, 2013.

97 D. H. Kim, D. Y. Oh, K. H. Park, Y. E. Choi, Y. J. Nam, H. A. Lee, S.-M. Lee and Y. S. Jung, *Nano letters*, 2017, **17**, 3013–3020.

98 X. Yu, Z. Bi, F. Zhao and A. Manthiram, *ACS applied materials & interfaces*, 2015, **7**, 16625–16631.

99 J.W. Park, K. Ueno, N. Tachinawa, K. Dokko and M. Watanabe, *Journal of Physical Chemistry C*, 2013, **117**, 4431-4440.

100 A. Unemoto, H. Ogawa, Y. Gambe and I. Honma, *Electrochimica Acta*, 2014, **125**, 386-394.

101 Z. Lin and C. Liang, *Journal of Materials Chemistry*, 2015, **3**, 936-58.

102 N. Angulakshmi and A.M. Stephan, *Frontiers in Energy Research*, 2015, **3**, Art. 17, p2.

103 L. Wang, J. Liu, S. Yuan, Y. Wang and Y. Xia, *Energy & Environment Science*, 2016, **9**, 224-231.

104 L. Wang and H.R**.** Byon**,** *Journal of Power Sources*, 2013, **236**, 207-214.

105 C. Wang, L. Zhang, H. Xie, G. Pastel, J. Dai, Y. Gong, B. Liu, E. D. Wachsman and L. Hu, *Nano Energy*, 2018, **49**, 58.